


 Open access • Journal Article • DOI:10.1088/1361-648X/AC0193

**Structure of disordered materials under ambient to extreme conditions revealed by synchrotron x-ray diffraction techniques at SPring-8-recent instrumentation and synergic collaboration with modelling and topological analyses. — [Source link](#) **

[Koji Ohara](#), [Yohei Onodera](#), [Motohiko Murakami](#), [Shinji Kohara](#)

**Institutions:** [Kyoto University](#), [ETH Zurich](#), [National Institute for Materials Science](#)

**Published on:** 20 Jul 2021 - [Journal of Physics: Condensed Matter](#) (IOP Publishing)

Related papers:

- [Structure of Disordered Materials Studied by High-Energy X-Ray Diffraction Technique](#)
- [The Disordered 3-Dimensional Structure Visualized by a Combination of High-energy Synchrotron X-rays and Computer Simulations](#)
- [X-ray diffraction and scattering on disordered systems using synchrotron radiation](#)
- [High-energy X-ray diffraction studies of disordered materials](#)
- [Requirements for X-ray structure analysis with modern synchrotron light sources](#)

Share this paper:    

View more about this paper here: <https://typeset.io/papers/structure-of-disordered-materials-under-ambient-to-extreme-1vpr4cb7x>

# Structure of disordered materials under ambient to extreme conditions revealed by synchrotron x-ray diffraction techniques at SPring-8—recent instrumentation and synergic collaboration with modelling and topological analyses

## Review Article

### Author(s):

Ohara, Koji; Onodera, Yohei; [Murakami, Motohiko](#) ; Kohara, Shinji

### Publication date:

2021-09-22

### Permanent link:

<https://doi.org/10.3929/ethz-b-000497102>

### Rights / license:

[Creative Commons Attribution 4.0 International](#)

### Originally published in:

Journal of Physics: Condensed Matter 33(38), <https://doi.org/10.1088/1361-648x/ac0193>

## Topical Review

# Structure of disordered materials under ambient to extreme conditions revealed by synchrotron x-ray diffraction techniques at SPring-8—recent instrumentation and synergic collaboration with modelling and topological analyses

Koji Ohara<sup>1</sup>, Yohei Onodera<sup>2,3</sup>, Motohiko Murakami<sup>4</sup> and Shinji Kohara<sup>3,4,\*</sup>

<sup>1</sup> Diffraction and Scattering Division, Japan Synchrotron Radiation Research Institute (JASRI), Sayo-gun, Hyogo 679-5198, Japan

<sup>2</sup> Institute for Integrated Radiation and Nuclear Science, Kyoto University, Sennan-gun, Osaka 590-0494, Japan

<sup>3</sup> Research Center for Advanced Measurement and Characterization, National Institute for Materials Science (NIMS), Sayo-gun, Hyogo 679-5148, Japan

<sup>4</sup> Department of Earth Science, ETH Zürich, Zürich 8092, Switzerland

E-mail: [KOHARA.Shinji@nims.go.jp](mailto:KOHARA.Shinji@nims.go.jp)

Received 23 December 2020, revised 16 March 2021

Accepted for publication 14 May 2021

Published 20 July 2021



### Abstract


The structure of disordered materials is still not well understood because of insufficient experimental data. Indeed, diffraction patterns from disordered materials are very broad and can be described only in pairwise correlations because of the absence of translational symmetry. Brilliant hard x-rays from third-generation synchrotron radiation sources enable us to obtain high-quality diffraction data for disordered materials from ambient to high temperature and high pressure, which has significantly improved our grasp of the nature of order in disordered materials. Here, we introduce the progress in the instrumentation for hard x-ray beamlines at SPring-8 over the last 20 years with associated results and advanced data analysis techniques to understand the topology in disordered materials.

Keywords: glass, liquid, x-ray diffraction, structure

(Some figures may appear in colour only in the online journal)

---

\* Author to whom any correspondence should be addressed.

 Original content from this work may be used under the terms of the [Creative Commons Attribution 4.0 licence](https://creativecommons.org/licenses/by/4.0/). Any further distribution of this work must maintain attribution to the author(s) and the title of the work, journal citation and DOI.

## 1. Introduction

The absence of translational periodicity and symmetry, and the very much present complexity in the structure of glassy, liquid, and amorphous materials make it difficult to understand the ordering of disordered materials. Indeed, as noted by Egelstaff in his review article in 1983 [1], determining the structure of disordered materials can be frustrating; although the underlying concepts have been known for a while, appropriate measurement methods for obtaining diffraction data of sufficient quality are usually not available. However, the advancement of instrumentation and measurement protocols makes it feasible to use quantum beam diffraction [x-ray diffraction (XRD) and neutron diffraction (ND)] techniques to reveal the structure of disordered materials at synchrotron and neutron facilities [2]. Moreover, a combination of diffraction measurement, advanced computer simulation, and topological analysis techniques enables us to understand the structure of disordered materials at both the atomistic and electronic levels [3, 4].

The synchrotron hard x-ray ( $E > 50$  keV) diffraction technique has become feasible with the arrival of the third-generation synchrotron sources and/or the introduction of advanced insertion devices (wigglers and undulators), leading to new approaches in the quantitative study of the structure of disordered materials. Poulsen *et al* [5] reported the first pair distribution function (PDF) analysis on silica glass in 1995 using synchrotron hard x-rays. They used hard x-rays from a wiggler at HASYLAB, Germany, to collect diffraction data up to scattering vector  $Q = 30 \text{ \AA}^{-1}$  [ $Q = (4\pi/\lambda) \sin \theta$  with  $2\theta$  being the scattering angle and  $\lambda$  the photon wavelength], providing a sufficient real-space resolution, since real-space resolution depends on the maximum  $Q$  value in a Fourier transform (see next section). After their landmark study, this technique has been widely applied to disordered materials from ambient to extreme conditions at the third-generation synchrotron radiation facilities, the European Synchrotron Radiation Facility (ESRF, France), the Advanced Photon Source (APS, USA), and Super Photon ring 8 GeV (SPring-8, Japan).

It is well known that ND with isotropic substitution [6] is effective for extracting element-specific partial correlations, since the scattering length from a neutron beam is different for each isotope. In contrast, anomalous x-ray scattering (AXS) [7], which utilizes the anomalous change in the atomic form factor of a specific element that occurs when the energy of incident x-rays is near an absorption edge of the element, is performed at the synchrotron radiation facilities.

In addition, advanced computer simulations and modelling techniques, such as reverse Monte Carlo (RMC) simulation [8] and empirical potential structure refinement [9], can be applied to high-quality diffraction data and element-specific data to model the three-dimensional atomic arrangement of disordered materials to understand the structure of disordered materials at both the atomistic and electronic levels. In this article, we report recent progress in the instrumentation for

hard x-ray beamlines and the dedicated diffractometers developed at SPring-8 in the last 20 years, as well as the recent developments of ancillary equipment, particularly for high temperature. We also address the advanced data analysis techniques using simulation and structure modelling to uncover the topology in disordered materials.

## 2. Method

### 2.1. Definition of total structure factor $S(Q)$ and real-space functions

In XRD measurements on materials containing  $n$  chemical species, structural information is contained in the Faber–Ziman [10] total structure factor  $S(Q)$ ,

$$S(Q) = 1 + \frac{1}{[\langle W(Q) \rangle]^2} \sum_{i=1}^n \sum_{j=1}^n c_i c_j w_i^*(Q) w_j(Q) [S_{ij}(Q) - 1], \quad (1)$$

where  $c_i$  is the atomic fraction of chemical species  $i$ ,  $w_i(Q)$  is a  $Q$ -dependent atomic form factor with dispersion terms and is a complex number, and  $S_{ij}(Q)$  is the partial structure factor,

$$\langle W(Q) \rangle = \sum_i c_i w_i(Q). \quad (2)$$

The corresponding real space information is contained in the reduced PDF  $G(r)$  that is obtained by a Fourier transform,

$$G(r) = \frac{2}{\pi} \int_{Q_{\min}}^{Q_{\max}} Q [S(Q) - 1] \sin(Qr) dQ, \quad (3)$$

where  $r$  is the distance in real space. The PDF  $g(r)$ , the total correlation function  $T(r)$ , and the radial distribution function RDF( $r$ ) are defined as follows:

$$g(r) = \frac{G(r)}{4\pi r \rho} + 1, \quad (4)$$

$$T(r) = G(r) + 4\pi r \rho = 4\pi r \rho g(r), \quad (5)$$

$$\text{RDF}(r) = rG(r) + 4\pi r^2 \rho = rT(r), \quad (6)$$

where  $\rho$  is the atomic number density. By using real-space functions, it is possible to obtain interatomic distances and coordination numbers.

### 2.2. Lineup of hard x-ray beamlines for disordered materials at SPring-8

In the last 20 years, we have developed the dedicated diffractometer and AXS spectrometer at the high-energy XRD beamline BL04B2 [11], the high-energy inelastic beamline BL08W [12], and the surface and interface structures beamline BL13XU [13]. Moreover, we have attempted several measurements on liquids and glasses under high pressure using a diamond anvil cell (DAC) at BL04B2 and the high-pressure research beamline BL10XU [14] using monochromatic hard

x-rays [15, 16], while many measurements on liquids and glasses under high temperature and high pressure have been performed using a combination of white x-rays and a multi-anvil press [17–19].

**2.2.1. Dedicated x-ray PDF diffractometer at BL04B2.** A dedicated x-ray PDF diffractometer for disordered materials at BL04B2 was built in 1999. The light source of BL04B2 is a bending magnet whose critical energy of 28.9 keV and single-bounce bent Si 111 and Si 220 crystals with a Bragg angle fixed to  $3^\circ$  provide 37.8, 61.7, and 113.3 keV x-rays. The details of the beamline are described in reference [11]. The advantages of our dedicated diffractometer are an extremely low background and high reliability of diffraction data, which are important factors in obtaining accurate PDF data [20–24].

The dedicated diffractometer for disordered materials has operated over 20 years at BL04B2. The detector of the first generation was intrinsic germanium (Ge) [20–22] and that of the second generation was triple-cadmium telluride (CdTe) [23]. The advantage of a Ge detector is supersensitivity, which is important in the high-diffraction-angle region, because the diffraction intensity is weak in the high-scattering-vector  $Q$  (high diffraction angle) region owing to the decay of the  $Q$ -dependent atomic form factors. The efficiency of the Ge detector (Mirion Technologies GL0515; the area and thickness of the detector are  $500 \text{ mm}^2$  and 15 mm, respectively) is comparable to that of the CdTe detector (AMPTEK X-123CdTe; the area and thickness of the detector are  $25 \text{ mm}^2$  and 1 mm, respectively) at 61 keV, but 1.8 times higher at 113 keV. In addition, the size of the detector element of Ge is much larger than that of CdTe. It was confirmed that approximately twice the gain is obtained with a Ge detector in comparison with a CdTe detector at 61 keV, suggesting that about a fourfold higher gain is obtained in the case of 113 keV. Another advantage of a semiconductor detector is high energy resolution to discriminate fluorescence from the sample and the signal of the higher harmonic reflections of the monochromator crystal. The energy resolution (FWHM) of CdTe detectors is better than 3.1 keV, whereas that of Ge detectors is better than 1.0 keV. The disadvantage of the Ge detector is the necessity to replenish the liquid nitrogen, which interrupts the measurement. On the other hand, the advantage of the CdTe detector is its small size, which is suitable to cover low-diffraction-angle regions where space is limited. Another advantage of the CdTe detector is that it adopts a Peltier device cooling system because of the small detector element. In the recent upgrade, we installed four CdTe detectors for low-diffraction-angle regions and three Ge detectors with an automated liquid nitrogen filling system for high-diffraction-angle regions. The typical setup of the upgraded diffractometer is shown in figure 1. The details of the upgraded diffractometer are described in reference [24].

**2.2.2. Area detector system for rapid data collection at BL08W.** An area detector system has recently been installed at BL08W. The light source of the beamline is an elliptical multipole

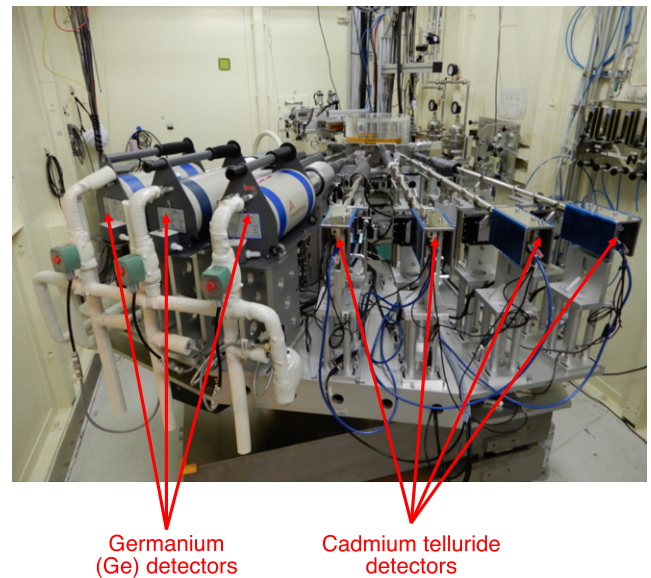


**Figure 1.** The hard x-ray PDF diffractometer installed at BL04B2. Reproduced with permission from [24].

wiggler with a critical energy of 42.7 keV at a 25.5 mm gap [25, 26]. The white x-rays emitted from the wiggler are monochromatized at 115.56 keV and focussed by an asymmetric Johann-type monochromator Si (400). The details of the beamline are available in reference [12].

Figure 2 shows a schematic illustration and a photograph of the detector system installed at BL08W. The detector system consists of a 4D slit, sample stage, beam stop (not shown in figure 2(a)), and amorphous (a-)Si flat panel detector (PerkinElmer, XRD1621CN3), as well as a collimator installed upstream of the 4D slit (figure 2(b)). The detector size is  $16'' \times 16''$  and the pixel size is  $200 \mu\text{m}$ . The scintillator material is caesium iodide. As can be seen in figure 2(b), the camera length from the sample position to the detector is variable between 300–800 mm. More detailed information is available in reference [27].

The  $Q$ -weighted total structure factors,  $Q[S(Q) - 1]$ , for silica glass measured by the rapid data collection system are shown in figure 3. It is confirmed that a 30 s measurement provides sufficient statistics at a high  $Q$  portion.

**2.2.3. Anomalous x-ray scattering spectrometer at BL13XU.** The AXS technique utilizes the anomalous change in the atomic form factor of a specific element that occurs when the energy of incident x-rays is near an absorption edge. The complex atomic form factor of an element is given as

$$f(Q, E) = f_0(Q) + f'(E) + if''(E), \quad (7)$$

where  $f_0(Q)$  is the energy-independent term, and  $f'(E)$  and  $f''(E)$  are the real and imaginary parts of the anomalous term, respectively.  $(Q, E)$  depends on the  $Q$ -dependent  $f_0(Q)$  in normal x-ray scattering, and the anomalous term is usually negligible. When the energy of incident x-rays approaches an absorption edge of an element,  $f'(E)$  has a large



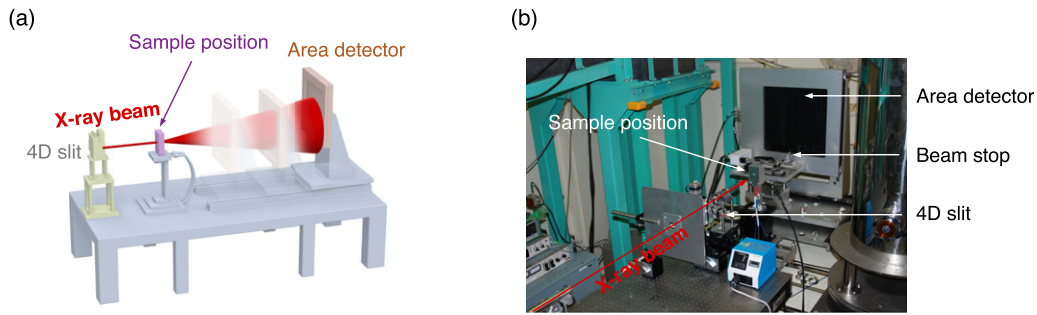


**Figure 2.** Schematic illustration (a) and photograph (b) of the area detector system for rapid data collection installed at BL08W. Reproduced from [27]. CC BY 4.0.

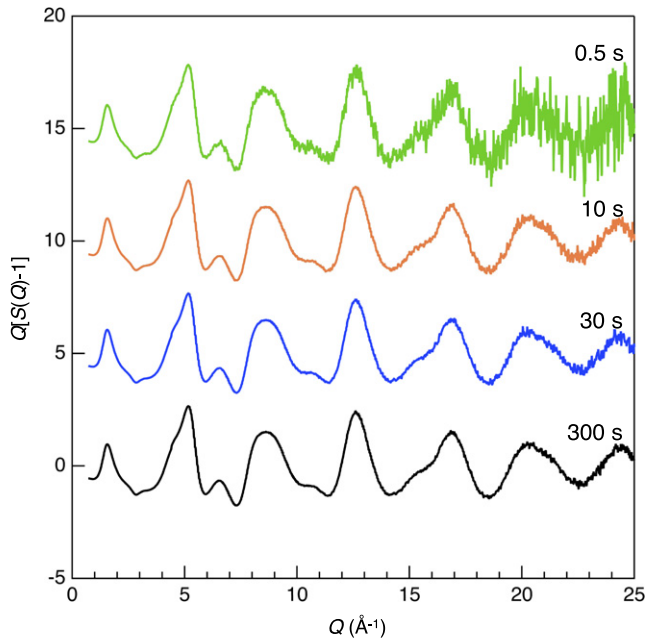


**Figure 3.** Typical diffraction data for silica glass measured at BL08W using the area detector system installed at BL08W. Reproduced from [27]. CC BY 4.0.

negative minimum and  $f''(E)$  changes abruptly near the absorption edge energy of each element. Therefore, it is possible to utilize the difference between two scattering data values,  $\Delta_i I(Q)$ , near an absorption edge of the  $i$ th element, where one spectrum is typically measured at  $\sim 30$  eV below the absorption edge ( $E_{\text{near}}$ ), while the other is measured at  $\sim 200$  eV below the absorption edge ( $E_{\text{far}}$ ). This differential spectrum is expressed as

$$\alpha_i \Delta_i I(Q, E_{\text{far}}, E_{\text{near}}) = \Delta_i [\langle f^2 \rangle - \langle f \rangle^2] + \Delta_i [\langle f^2 \rangle] \Delta_i S(Q), \quad (8)$$

where  $\alpha_i$  is a normalization constant and  $\Delta_i [ ]$  is the difference between the values in brackets at the energies of  $E_{\text{far}}$  and  $E_{\text{near}}$ . The  $\Delta S(Q)$  functions are given by a linear combination of  $S_{ij}(Q)$  as

$$\Delta_i S(Q) = \sum_{i=1}^N \sum_{j=1}^N w_{ij}(Q, E_{\text{far}}, E_{\text{near}}) S_{ij}(Q), \quad (9)$$

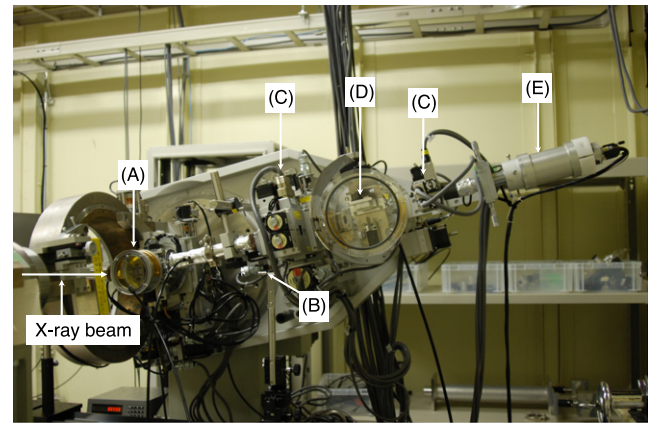


**Figure 4.** The AXS spectrometer attachments installed at BL13XU. Reproduced with permission from [23]. (A) Vacuum chamber (sample), (B) beam stop, (C) slits, (D) LiF analyzer crystal, and (E) NaI (Tl) scintillation detector.

where the weighting factors are given by

$$w_{ij}(Q, E_{\text{far}}, E_{\text{near}}) = c_i c_j \frac{\Delta_i [f_i f_j^*]}{\Delta_i [\langle f \rangle^2]}. \quad (10)$$

It is notable that compared with  $S(Q)$ ,  $\Delta S_i(Q)$  enhances the contribution of the  $i$ th-element-related partial structure factors and hence can suppress those of other partials.

The dedicated AXS spectrometer was developed at BL13XU is an in-vacuum undulator, and a cryogenic Si 111 double-crystal monochromator has been installed [13]. Figure 4 shows the AXS spectrometer attachments installed on the six-circle diffractometer (Kohzu Precision Co. Ltd., TDT-17) at BL13XU, where the diffractometer operates as a high-resolution spectrometer with a LiF 200 analyzer crystal. The spectrometer consists of the six-circle diffractometer, a vacuum sample chamber, receiving slits, a beam stop, an analyzer crystal, and a NaI(Tl) scintillation detector.

The energy resolution ( $\Delta E/E$ ) of an analyzer crystal is given by

$$\frac{\Delta E}{E} = \frac{\Delta \theta}{\tan \theta_B}, \quad (11)$$

where  $\Delta \theta$  and  $\theta_B$  are the rocking-curve width and Bragg angle, respectively. By choosing an analyzer crystal with a sufficient

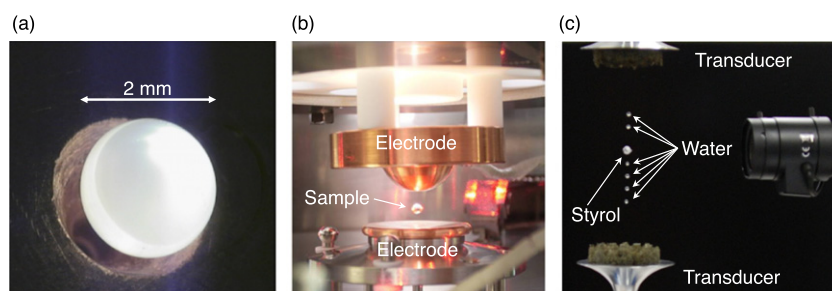


**Figure 5.** Photographs of aerodynamic levitation (a), electrostatic levitation (b), and acoustic levitation (c) instruments. Reproduced with permission from [23].



**Figure 6.** Typical DAC high-pressure apparatus with a large conical angular aperture.

rocking-curve width, the fluorescence and Compton scattering can be discriminated with sufficient statistics. Moreover, it should be pointed out that a LiF crystal is a low-cost product. A vacuum chamber is installed to avoid scattering by air around the sample. The vacuum chamber is also useful for hygroscopic samples. High energy resolution is an important factor in precise AXS measurements since fluorescence is induced by incident x-rays while measuring near the absorption edge. The energy resolution of the LiF 200 crystal is approximately 12 eV in FWHM at 12 keV, which allows the contributions from fluorescence and Compton scattering to be discriminated. Furthermore, the energy resolution of the crystal is approximately seven times better than that obtained by sagittal focussing of a cylindrical mosaic graphite crystal [28].

### 2.3. Development of ancillary equipment for high temperature and high pressure

We have developed ancillary equipment over the last 20 years: fully automatic sample changers [22] and the conventional high temperature furnace [22]. In this section, we focus on the development of the levitation furnace [29] for containerless liquids in a wide temperature range. Moreover, high-pressure XRD measurements using a DAC for the structural studies of oxide glass under ultrahigh pressure are introduced.

#### 2.3.1. Lineup of levitation techniques developed at SPring-8.

The use of hard x-rays at the third-generation synchrotron

radiation sources makes it possible to perform the measurements under extreme conditions, and hence, relevant levitation techniques have been developed [29]. Levitation methods allow enhanced glass formation owing to the elimination of unfavorable extrinsic heterogeneous nucleation. They also enable experiments on high-temperature liquids and deeply undercooled liquids without contamination of container materials. Recently, the use of levitation techniques to study liquids and the synthesis of glasses from undercooled liquids has been of particular interest for understanding the structure of nonglass-forming liquids and the process of glass formation. Three levitation techniques, aerodynamic (conical nozzle) levitation [29, 30], electrostatic levitation [27, 31, 32], and acoustic levitation [33], are available (figure 5) at the SPring-8 beamlines.

In the aerodynamic levitation technique [29], a sample is levitated by a gas flow in a convergent–divergent conical nozzle, where Bernoulli force pushes the sample back to the axis of the nozzle. The levitated samples can be heated by a continuous wave CO<sub>2</sub> laser. The conditions for levitation are derived from the law of momentum conservation applied to a control volume that contains the sample:

$$\int \left[ \frac{1}{2} \rho_G \mu^2 + p \right] dA = Mg, \quad (12)$$

where  $\rho_G$ ,  $\mu$ , and  $p$  are the gas density, gas flow velocity, and pressure, respectively, and  $Mg$  is the weight of the sample. The integral is evaluated over the surface  $A$  of the control volume.

The electrostatic levitation technique [31] is very useful for the measurement of diffraction and thermophysical properties. A charged liquid drop is levitated between a pair of electrodes, and it is free from obstacles, such as the nozzle or coils in other levitators. Moreover, to avoid electrical breakdown when applying a high voltage between the two electrodes, electrostatic levitators must be operated under either a high vacuum or pressurized atmosphere ( $\sim 0.4$  MPa). High-vacuum conditions are useful for avoiding the unfavorable oxidation of melts.

Acoustic levitation was optimized to levitate low-temperature liquids typically in a cryojet. This technique has potential for new applications of low-temperature liquids in pharmaceutical [34] and engineering sciences. A single-axis acoustic levitator [33] levitates liquid and solid drops of

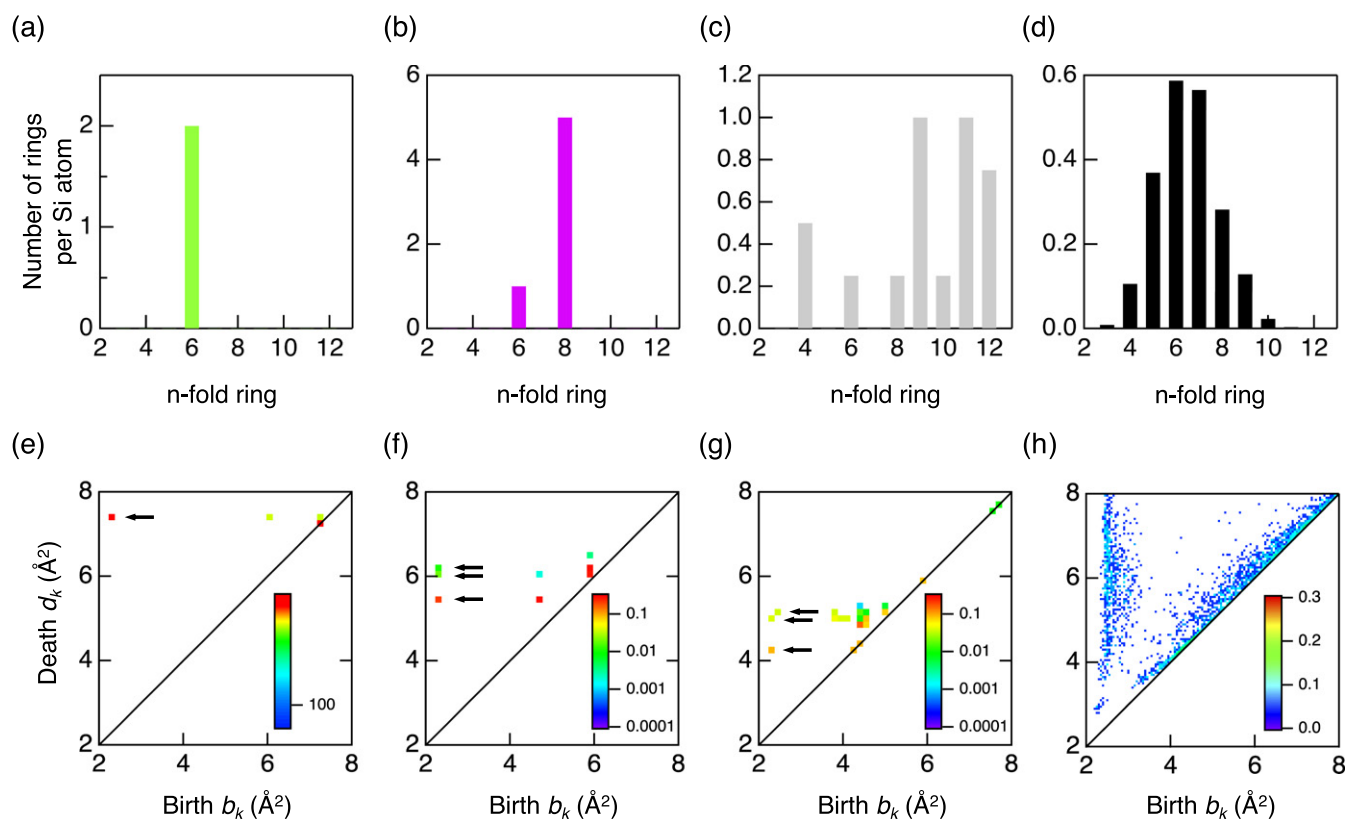


**Figure 7.** Primitive ring statistics for (a)  $\alpha$ -cristobalite, (b)  $\alpha$ -quartz, (c) coesite, and (d) g-SiO<sub>2</sub> [4]. Si-centric PDs for (e)  $\alpha$ -cristobalite, (f)  $\alpha$ -quartz, (g) coesite, and (h) g-SiO<sub>2</sub>. Reproduced from [4]. [CC BY 4.0](https://creativecommons.org/licenses/by/4.0/).

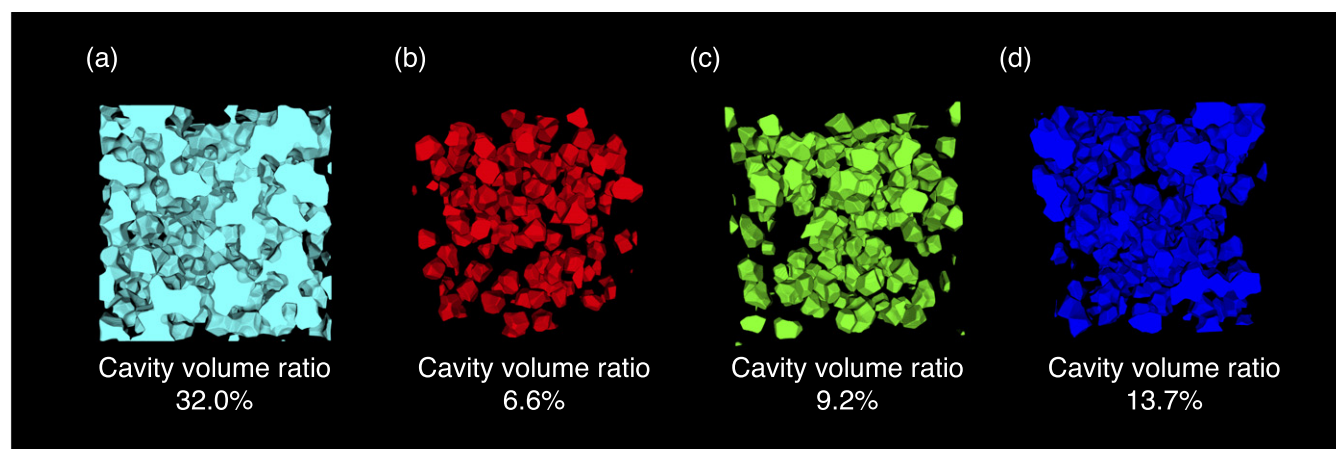


**Figure 8.** Visualization of surface cavities in the 22.7R<sub>2</sub>O–77.3SiO<sub>2</sub> glasses ( $R = \text{Na, K}$ ). Cyan: SiO<sub>2</sub> glass; red: Na100 glass; green: Na50K50 glass; blue: K100 glass. Reproduced from [48]. [CC BY 4.0](https://creativecommons.org/licenses/by/4.0/).

1–3 mm diameter in the temperature range of  $-40$  to  $+40$  °C. The levitator consists of two acoustic transducers and an acoustic power supply that controls the acoustic intensity and relative phase of the two transducers. The acoustic transducers are operated at a resonant frequency of  $\sim 22$  kHz and produce sound pressure levels of up to 160 dB. The force applied by the acoustic field can be modulated to excite oscillations in a sample drop.

**2.3.2. Hard x-ray diffraction measurement on oxide glass under ultrahigh pressure using DAC.** Angle-dispersive XRD measurements for oxide glass *in situ* under an extremely high-pressure condition approaching 200 GPa are possible in a DAC high-pressure apparatus at BL10XU [16]. An incident x-ray beam is monochromatized, using a diamond double-crystal monochromator, to an incident energy of  $\sim 50$  keV. The x-ray beam is collimated to  $\sim 40$   $\mu\text{m}$  in diameter, and the XRD



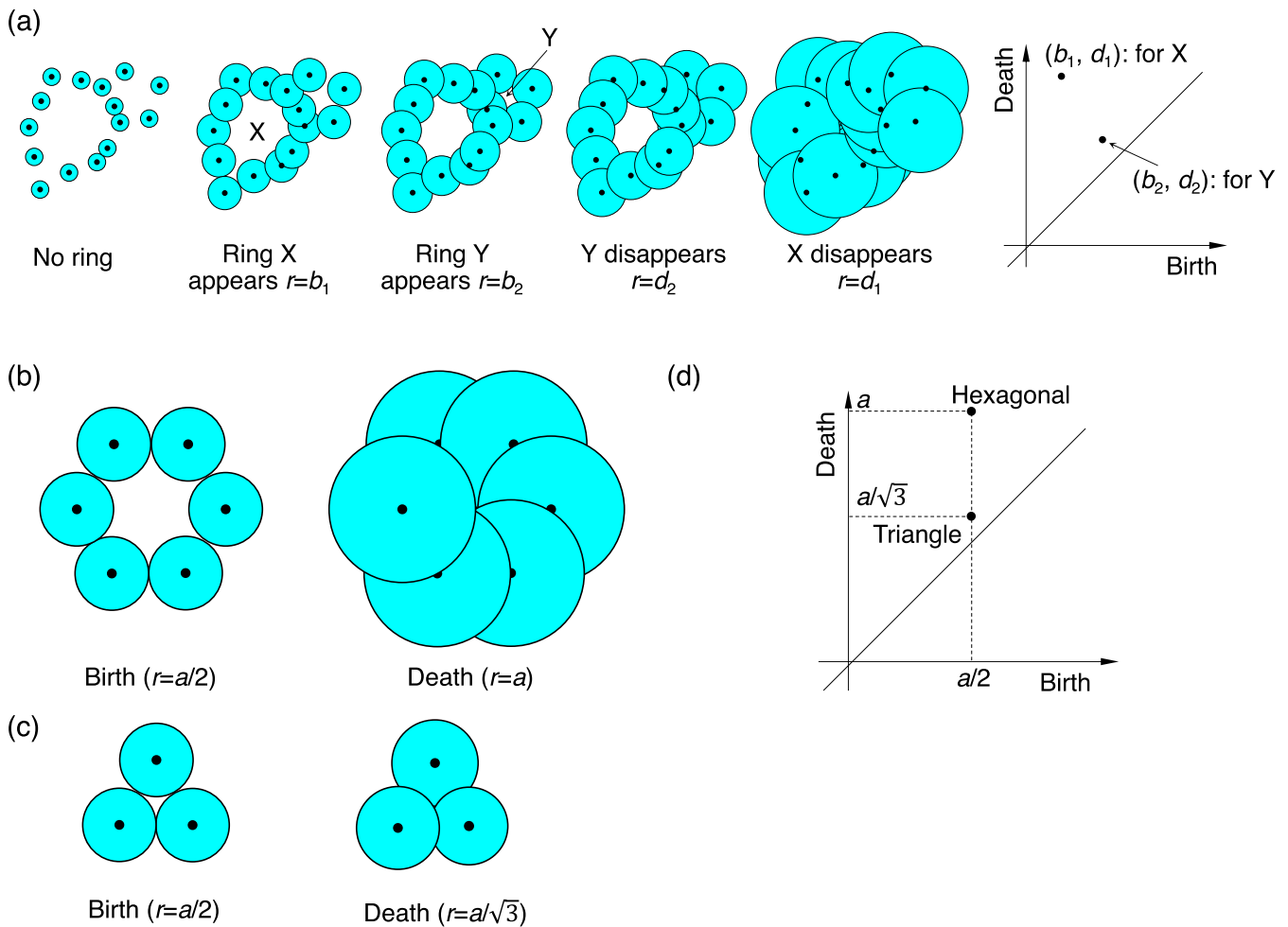


**Figure 9.** Persistent homology and typical PDs. Reproduced with permission from [49]. (a) The increasing sequence of spheres for input data (left). The PD (right) is obtained as a histogram counting the number of rings on the birth–death plane. (b) and (c) The appearance and disappearance of a ring for a regular hexagon/triangle. (d) The pairs of birth and death radii for hexagon and triangle in the one-dimensional PD.

pattern of the sample in a DAC is measured using an image plate (Rigaku-RAXIS IV++), which has the dimensions of  $3000 \times 3000$  (pixel) with a pixel size of  $100 \times 100 \mu\text{m}$ . Integration of the full-circle scattered x-ray images provides conventional one-dimensional profiles. The  $Q$  value was calibrated using the diffraction pattern of crystalline  $\text{CeO}_2$ . More details of the beamline are described in reference [14]. The DAC with a large conical angular aperture ( $\sim 70\text{--}80^\circ$ ) has been used to gain a wider range of  $Q$  (figure 6). A prepressed plate of oxide glass sample is loaded into a hole drilled in the rhenium gasket without a pressure-transmitting medium. The glass sample in the DAC is then compressed with  $150\text{--}300 \mu\text{m}$  culet diamond anvils. To subtract the background signals arising mainly from the Compton scattering of the diamond anvils, the background XRD pattern is collected for each experimental run after decompression from an empty rhenium gasket hole in a DAC without the compressed sample. Pressure can be determined by Raman spectroscopic measurements with the  $T_{2g}$  mode of the diamond anvil [35] or a ruby fluorescence pressure scale [36].

## 2.4. Topological analyses

In this section, we present three important novel topological analysis tools for glassy materials: ring statistics, cavity, and persistent homology analyses. However, well-established simpler methods, such as calculating the distributions of bond angles and dihedral angles, may still be widely applied.

**2.4.1. Ring statistics.** The history of ring statistics calculations is relatively long. The most widely used computer code was developed by Roux and Jund [37, 38]. There is a variety of criteria for a ring: King [39], shortest path [40, 41], primitive [42, 43] (or irreducible [44]), and strong rings [42, 43]. Details are described in references [37, 38]. Figures 7(a)–(d) show primitive ring statistics in  $\text{SiO}_2$  crystals,  $\alpha$ -cristobalite ( $d = 2.327 \text{ g cm}^{-3}$ ),  $\alpha$ -quartz ( $d = 2.655 \text{ g cm}^{-3}$ ), and coesite ( $d = 2.905 \text{ g cm}^{-3}$ ), together with that of glassy (g)- $\text{SiO}_2$  ( $d = 2.2 \text{ g cm}^{-3}$ ) obtained from molecular dynamics (MD)–RMC modelling [8].  $\alpha$ -cristobalite shows only sixfold rings consisting of six  $\text{SiO}_4$  tetrahedra, while  $\alpha$ -quartz has a large fraction of eightfold rings in addition to sixfold rings [4]. On the other hand, both coesite and g- $\text{SiO}_2$  exhibit a distribution of different

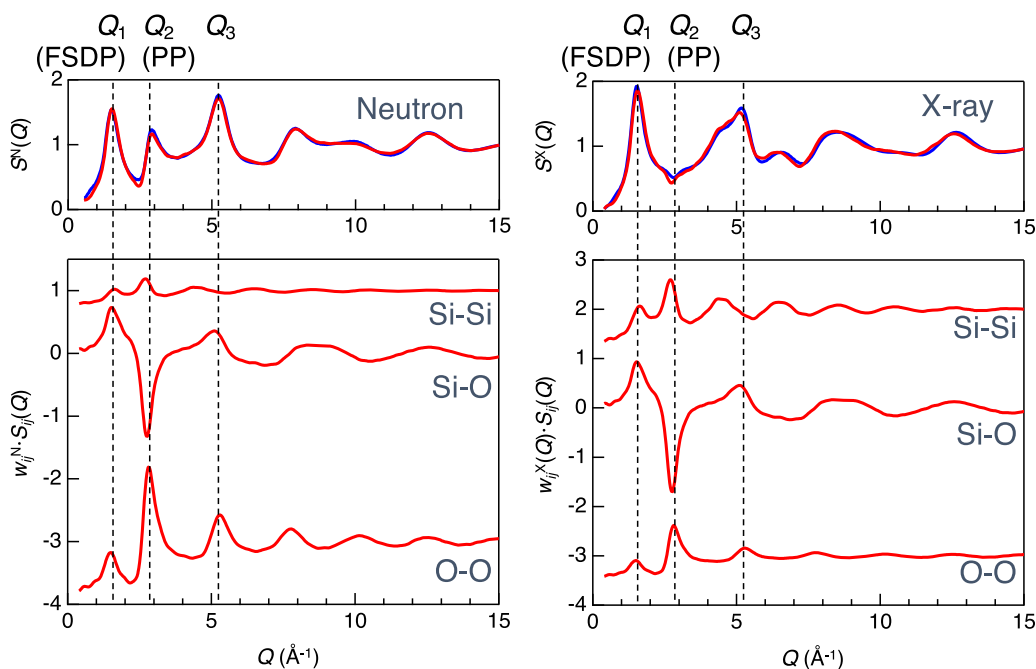


**Figure 10.** Neutron- (left), [77] ISIS Disordered Materials Database, <http://www.alexhannon.co.uk> and x-ray- (right) weighted total structure factors, reproduced from [4]. CC BY 4.0,  $S(Q)$ , for g-SiO<sub>2</sub> together with the partial structure factors,  $S_{ij}(Q)$ , obtained from MD-RMC modelling.

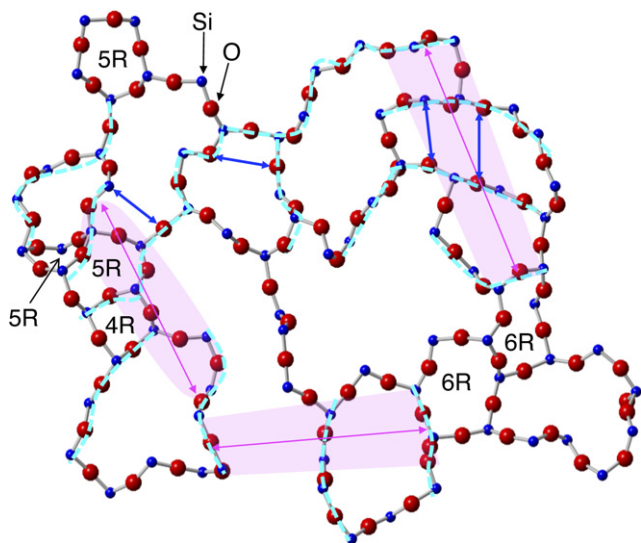


**Figure 11.** MD-RMC-generated atomic configuration for g-SiO<sub>2</sub>. Reproduced from [4]. CC BY 4.0. The thickness of the cell is approximately 9 Å and only the atoms belonging to the network are shown.

size rings, which is a sign of topological disorder according to Gupta and Cooper [45].

**2.4.2. Cavity analysis.** The distribution of cavities in glassy materials is an important property for understanding physicochemical properties. Although positron annihilation lifetime spectroscopy (PALS) has been employed to perform a direct observation of the behaviour of cavities [46], the calculation of the distribution of cavities on the basis of atomic configurations obtained by computer modelling becomes

important. Heimbach *et al* have recently developed a dedicated code for cavity analysis, in which it is possible to calculate cavity distributions [47]. Figure 8 shows the modification of cavity distributions in the 22.7R<sub>2</sub>O–77.3SiO<sub>2</sub> (R = Na, K) alkali silicate glasses together with SiO<sub>2</sub> data [48]. Note that the absolute value of cavity volume depends on the definition of the minimum size of a cavity, which makes it difficult to compare the calculated cavity volume with results from PALS.

**2.4.3. Persistent homology analysis.** Recently, topological data analysis has rapidly progressed and has provided several tools for analyzing multiscale data in physical and biological fields [49]. Following the landmark study of Hirata *et al* [50], Hiraoka *et al* applied persistent homology for disordered materials to understand the homology of rings, a feature that cannot be detected by conventional ring statistics analysis [49]. This mathematical tool, based on the persistence diagram (PD), was developed to capture the shapes of multiscale data. The input to the PDs is atomic configurations and the output is expressed as 2D histograms. Then, specific distributions such as curves and islands in the PDs identify meaningful shape characteristics of the given atomic configuration.

The homology of atomic configurations can be investigated using the PDs obtained with the HomCloud software package [51]. Given a set of points in space, persistent homology captures its topological multiscale structures, and the structures identified are compactly expressed in the PD. The construction of the PD follows the process schematically depicted in figure 9(a). We first replace each point with a sphere and increase the radius from zero to a sufficiently large value; this corresponds to the changing resolution of input  $x, y$ ,

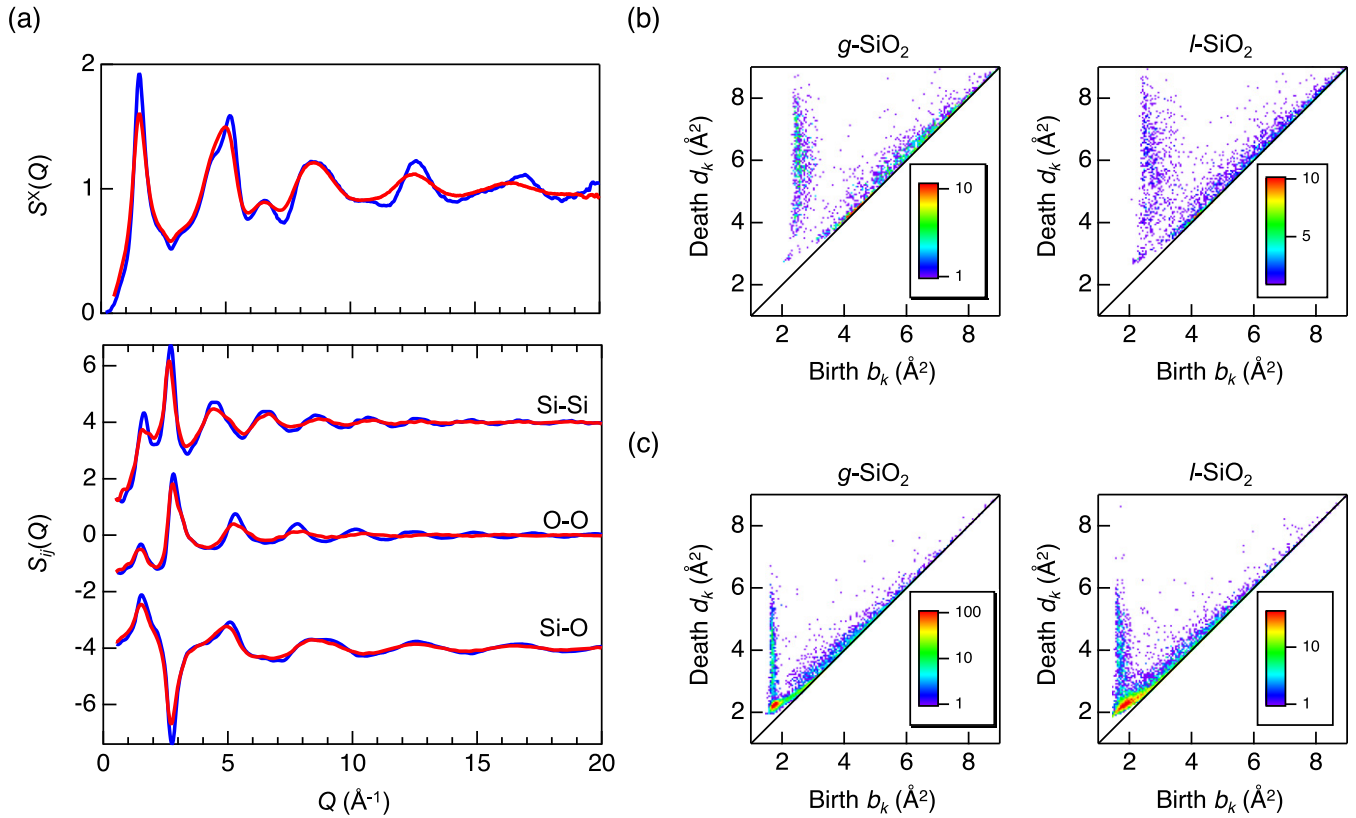


**Figure 12.** (a) X-ray total structure factors (top, reproduced from [4], CC BY 4.0),  $S^X(Q)$ , for  $g\text{-SiO}_2$  [4] and  $l\text{-SiO}_2$  (2323 K) [86] together with the MD-RMC-generated partial structure factors (bottom, reproduced from [4], CC BY 4.0),  $S_{ij}(Q)$ , for  $g\text{-SiO}_2$  (blue curves) and  $l\text{-SiO}_2$  (red curves, 2323 K). Si-centric PD (b) for  $g\text{-SiO}_2$  and  $l\text{-SiO}_2$ . O-centric PD (c) for  $g\text{-SiO}_2$  and  $l\text{-SiO}_2$ . Reproduced from [4], CC BY 4.0.

$z$  coordinates of atoms. Then, we record the pair of radii ( $b$ ,  $d$ ) at which a ring in a specific location appears (birth) and disappears (death), respectively. The PD is a histogram of the birth/death plane with counts of rings at the coordinates ( $b$ ,  $d$ ). This construction enables one to not only count the number of rings, but also characterize their shapes on a multiscale, by observing the characteristic shapes of the diagrams themselves.

Typical examples of birth/death pairs for typical regular structures are shown in figures 9(b)–(d). For a regular hexagonal arrangement of points in which the distance between points is  $a$ , the ring appears at radius  $a/2$  and disappears at radius  $a$ , as shown in figure 9(b). For a regular triangular configuration, the ring appears at  $a/2$  and disappears at  $\sqrt{1/3}a \approx 0.577a$ , as shown in figure 9(c). The one-dimensional PD for regular hexagonal/triangular points is shown in figure 9(d). In this article, PDs are being used to investigate rings and polyhedral formations in atomic configurations. We also note that the detected rings are recorded during the computation of the diagrams, and hence, we can explicitly identify their geometric shapes.

Figures 7(e)–(h) show the Si-centric PDs calculated from the crystal structures for  $\alpha$ -cristobalite,  $\alpha$ -quartz, and coesite, together with that of  $g\text{-SiO}_2$  obtained from MD-RMC modelling [4]. A systematic change in the Si-centric PDs with density is observed for the crystalline phases in figures 7(e)–(g). In contrast to the crystalline phases, the PD for  $g\text{-SiO}_2$

has a vertical profile along the death axis at  $b_k \sim 2.2 \text{\AA}^2$ , which is considered to be a signature of the formation of a  $-\text{Si}-\text{O}-\text{Si}-\text{O}-$  glass network [4, 48]. The Si-centric PDs and primitive ring size distributions shown in figure 7 provide us with comprehensive topological information, because ring size distribution analysis is sensitive to the ring size, whereas PDs make it possible to know the shape of rings. Since all forms of silica have corner-sharing  $\text{SiO}_4$  tetrahedral motifs, a comparison of  $\alpha$ -cristobalite,  $\alpha$ -quartz, and coesite with  $g\text{-SiO}_2$  in the Si-centric PDs suggests that glass has not only homology with a crystalline phase of comparable density ( $\alpha$ -cristobalite), but also homology with higher-density crystalline phases ( $\alpha$ -quartz and coesite). It is known that  $g\text{-SiO}_2$  has a distribution of ring sizes (topological disorder [45], see figure 7(d)) [52, 53] but figures 7(a)–(c) indicate that crystalline phases exhibit topological disorder with increasing density because ring size distributions become broad with increasing density. Moreover, both  $\alpha$ -quartz and coesite have large rings in spite of small death values, suggesting that these rings are unusually buckled. It is concluded on the basis of a combination of PD analysis and conventional ring statistical analysis, that the vertical profile along the death axis observed in the Si-centric PD for  $g\text{-SiO}_2$  is the result of disorder, because the small death value in the glass implies that the arrangement of  $\text{SiO}_4$  tetrahedra is locally more densely packed in the glass than in  $\alpha$ -cristobalite, whose density is comparable to that of  $g\text{-SiO}_2$ .

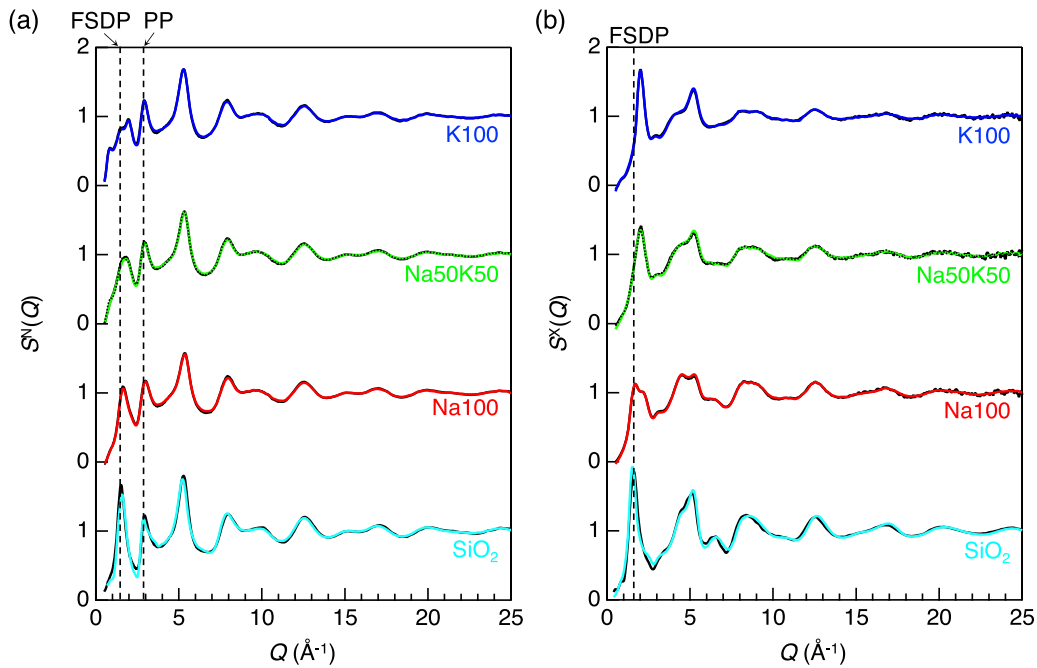


**Figure 13.** (a) Neutron total structure factors,  $S^N(Q)$ , and (b) x-ray total structure factors,  $S^X(Q)$ , for a series of the  $R_2O-SiO_2$  glasses ( $R = Na, K$ ). Reproduced from [48]. CC BY 4.0. Black solid curve, experimental data; coloured curve, MD-RMC model. Average experimental  $S^{N,X}(Q)$  for the Na50K50 glass calculated using the Na100 glass and K100 glass data are plotted as a dashed black curve.

### 3. Discussion

Recent scientific activities on disordered materials using XRD and ND techniques are reviewed in several articles [2, 54, 55]. In this section, we review recent structural studies on the structure of glassy, liquid and amorphous materials by diffraction techniques combined with computer simulations aided by topological analyses [4]. Over the last 20 years, we have been working on the structure of disordered materials, oxide glasses [48, 53, 56–59], amorphous oxide materials [60–62], chalcogenide fast phase-change materials [63–66], metallic glasses [67], water [68], high-temperature oxide melt [69–71], densified glass [72], and other functional materials [73, 74].

#### 3.1. Glassy and liquid $SiO_2$

Silica ( $SiO_2$ ) can be classified as a glassformer according to Zachariassen [75] and Sun [76], and hence, g- $SiO_2$  is one of the most important glassy materials in both fundamental and engineering sciences. The structure of g- $SiO_2$  has been studied widely by both experimental and theoretical approaches [54].

Figure 10 shows neutron-weighted,  $S^N(Q)$  [77], and x-ray-weighted,  $S^X(Q)$  [4], total structure factors of g- $SiO_2$  together with the partial structure factors,  $S_{ij}(Q)$ , obtained by MD-RMC modelling [4]. A three-peak [ $Q_1$  (FSDP),  $Q_2$  (PP), and  $Q_3$ ] structure [78] is observed in  $S^N(Q)$ , but a PP cannot be observed in  $S^X(Q)$  owing to the low weighting factor of the oxygen–oxygen correlation for x-rays.

It is well known that the short-range structure in g- $SiO_2$  is a  $SiO_4$  tetrahedron, and the interconnections of tetrahedra form a network with shared oxygen atoms at the corner. This polyhedral motif is manifested by the FSDP and the PP in  $S(Q)$

[78]. The FSDP was first discussed in 1976 [79], although it appears that the name ‘FSDP’ was first used by Phillips in 1981 [80]. An interpretation of diffraction peaks, including the FSDP, was attempted in the 1980s [80, 81] and details are discussed in several papers [82–86]. It is known that the FSDP of silica glass is related to the formation of a random network, as suggested by Zachariassen [75], and the model was extended to silicate glasses, as illustrated in figure 7 of reference [86], by Mei *et al.* It was confirmed that intermediate-range ordering (IRO) arises from the periodicity of boundaries between successive small cages in the network, formed by connected regular  $SiO_4$  tetrahedra with shared oxygen atoms at the corners. The IRO is thus associated with the formation of a ring structure and cavities [48, 72]. The second maximum, the PP, reflects the size of the local-network-forming motif, whereas the FSDP indicates the arrangement of these motifs on an intermediate range, according to Zeidler and Salmon [87]. Another interpretation of the FSDP has recently been proposed by Shi and Tanaka, who discussed local tetrahedral ordering in covalent liquids and glasses [88]. Since the origin of the FSDP has been discussed for a long time, as mentioned above, it is possible to estimate the periodicity and correlation length given by  $2\pi/Q_{FSDP}$  of  $\sim 4.15$  Å and  $2\pi/\Delta Q_{FSDP}$  of  $\sim 9.9$  Å for g- $SiO_2$ . These periodicity and correlation length are visible in the atomic arrangement obtained by MD-RMC modelling (see figure 11) [4].

The experimental  $S^X(Q)$  (upper) and MD-RMC-generated Faber–Ziman partial structure factors,  $S_{ij}(Q)$  (lower), of g- $SiO_2$  (blue curves) and l- $SiO_2$  (red curves) [89] are shown in figure 12(a). The liquid data were measured at 2323 K ( $T/T_g = 1.57$ , glass-transition temperature ( $T_g$ ) is 1482 K [90]). Although the peaks are broader, it appears that the FSDP



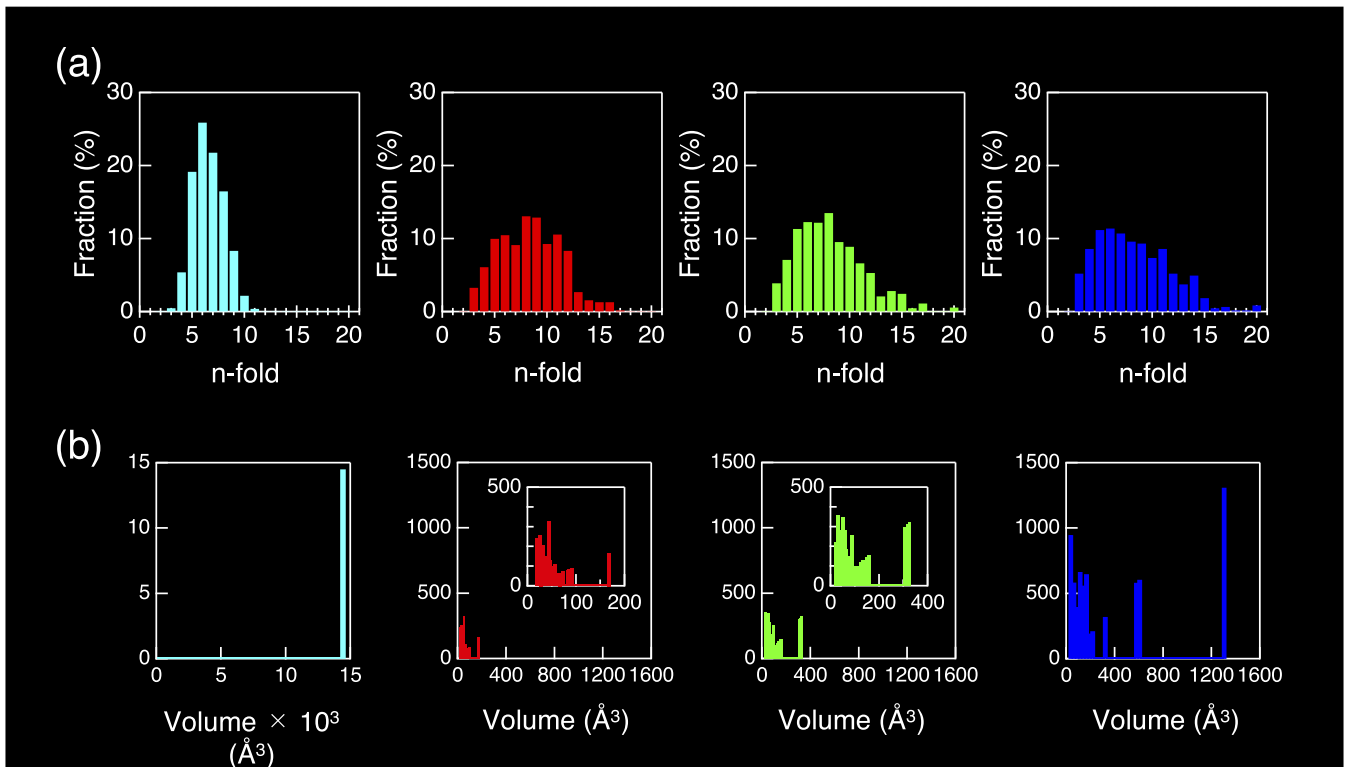


**Figure 14.** (a) Primitive ring statistics and (b) weighted surface cavity histograms for a series of the  $22.7R_2O-77.3SiO_2$  glasses ( $R = Na, K$ ). Reproduced from [48]. [CC BY 4.0](#). Cyan:  $SiO_2$  glass; red: Na100 glass; green: Na50K50 glass; blue: K100 glass. The insets highlight the distributions of small cavities.

is still dominant in the liquid. Mei *et al* [89] reported that the FSDP is largely intact in the liquid and there is no significant change in its position. Recently, Masai *et al* have reported that the position of the FSDP does not change between glasses prepared at different fictive temperatures [91]. Both the Si- and O-centric PDs, shown in figures 12(b) and (c), and the x-ray  $S(Q)$  (top) and the partial structure factors,  $S_{ij}(Q)$  (bottom), in figure 12(a) show only small differences between the glassy and liquid phases, suggesting that the  $SiO_4$  network with corner-sharing is very massive even in the liquid phase [92]. In addition, it is known that the density changes between liquid ( $d = 2.1 \text{ g cm}^{-3}$ ) and glass ( $d = 2.2 \text{ g cm}^{-3}$ ) smoothly across the glass transition and the difference is small. This feature can be reasonably well understood from the very high viscosity of l- $SiO_2$  [93], and hence, it is consistent with the concept of a ‘strong liquid’, as proposed by Angell [94].

### 3.2. $R_2O-SiO_2$ glass ( $R = Na, K$ )

It is well known that alkali mixing causes several unusual phenomena; that is, when an alkali ion is gradually replaced by another one, some physical properties vary in an extremely nonlinear manner. For instance, a composition containing equally mixed alkali ions has a pronounced maximum electrical resistivity and a substantially lower viscosity as a concave function of the alkali content, although the variation in the molar volume has an almost linear relationship with the alkali content [95].

The origin of the mixed alkali effect has been studied widely by many experimental and theoretical techniques [96]. A landmark study using RMC modelling based on ND and NMR data, reported by Wicks *et al* in 1997 [97], revealed that the modified random network (MRN) theory suggested by Greaves [98] is consistent with the data set used in reference [97]. Very recently, Onodera *et al* have revisited this topic with the aim of revealing the origin of the mixed alkali effect on the basis of topology that is hidden in the pairwise correlations [48].

Figure 13 shows the neutron and x-ray structure factors,  $S^{N,X}(Q)$ , of the alkali silicate glasses and  $SiO_2$  glass. A sharp FSDP is observed at  $Q \sim 1.5 \text{ \AA}^{-1}$  in  $S^{N,X}(Q)$  for  $SiO_2$  glass, whereas the FSDP becomes broader when alkali ions are added. The FSDP also appears in  $S^N(Q)$  for the alkali silicate glasses, but the shape of the peak is very complicated. Indeed, an extra peak is observed at  $Q \sim 0.8 \text{ \AA}^{-1}$  in the case of the K100 glass. On the other hand, the FSDP is not visible in  $S^X(Q)$  for either the Na50K50 or K100 glasses, because of the large weighting factors of potassium for x-rays. The PP is found only in  $S^N(Q)$  because the PP in silicate glasses is considered to reflect an oxygen–oxygen correlation that is easily detected by neutrons. It is worth noting that the average of the diffraction profiles of the Na100 and K100 glasses (black broken curve) is almost identical to the experimental data for the Na50K50 glass (green curve) for both  $S^N(Q)$  and  $S^X(Q)$ , implying that the mixed alkali effect cannot be detected easily in the diffraction data.

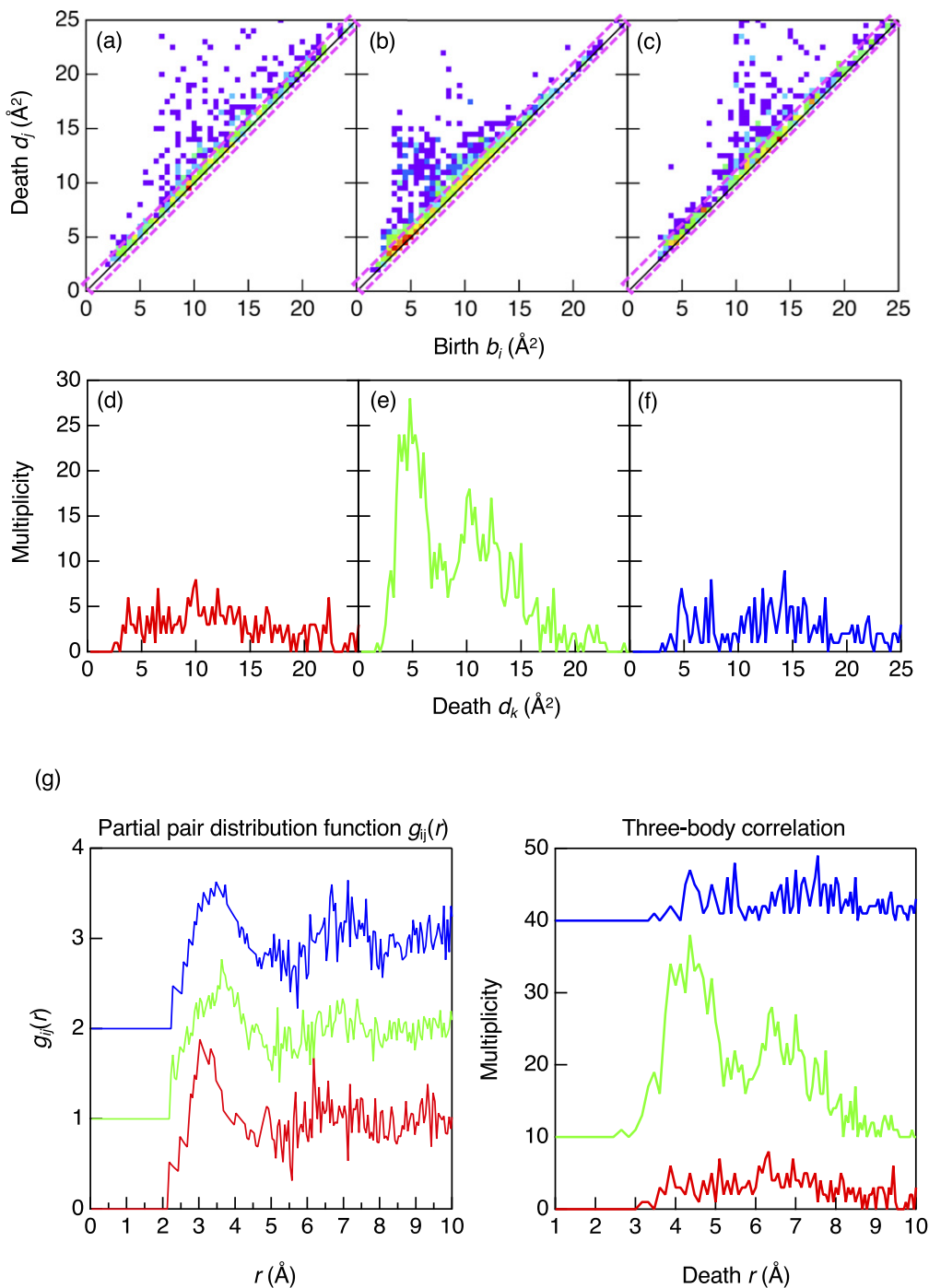


**Figure 15.** (a) Na-centric, (b) Na/K-centric, and (c) K-centric PDs for the Na50K50 glass. The boxed regions follow the diagonal, and the associated profiles are plotted for (d) Na-centric, (e) Na/K-centric, and (f) K-centric. (g) Partial PDFs,  $g_{ij}(r)$ , and three-body correlations extracted from the PDs. Reproduced from [48]. CC BY 4.0.

Therefore, it is necessary to analyse the MD-RMC-generated atomistic configurations to extract structural information. Figure 14(a) depicts the primitive (Si–O)<sub>n</sub> ring statistics. It is well known that glassy SiO<sub>2</sub> has a broad ring size distribution [4, 53], although sixfold rings, the only possible ring structure in the crystalline phase with comparable density ( $\alpha$ -cristobalite), are dominant. This broad distribution is the result of topological disorder according to Gupta and Cooper

[45], and hence, this is a very important characteristic of the glass. In the case of alkali silicate glasses, we can see a broader distribution due to the introduction of alkali ions that break down the Si–O network, which is consistent with findings of previous studies [97, 99]. The cavity surfaces are visualized in figure 8. SiO<sub>2</sub> glass, which yields the largest cavity volume ratio of 32%, exhibits a string-like cavity. The cavity volume ratio in the alkali silicate glasses increases monotonically

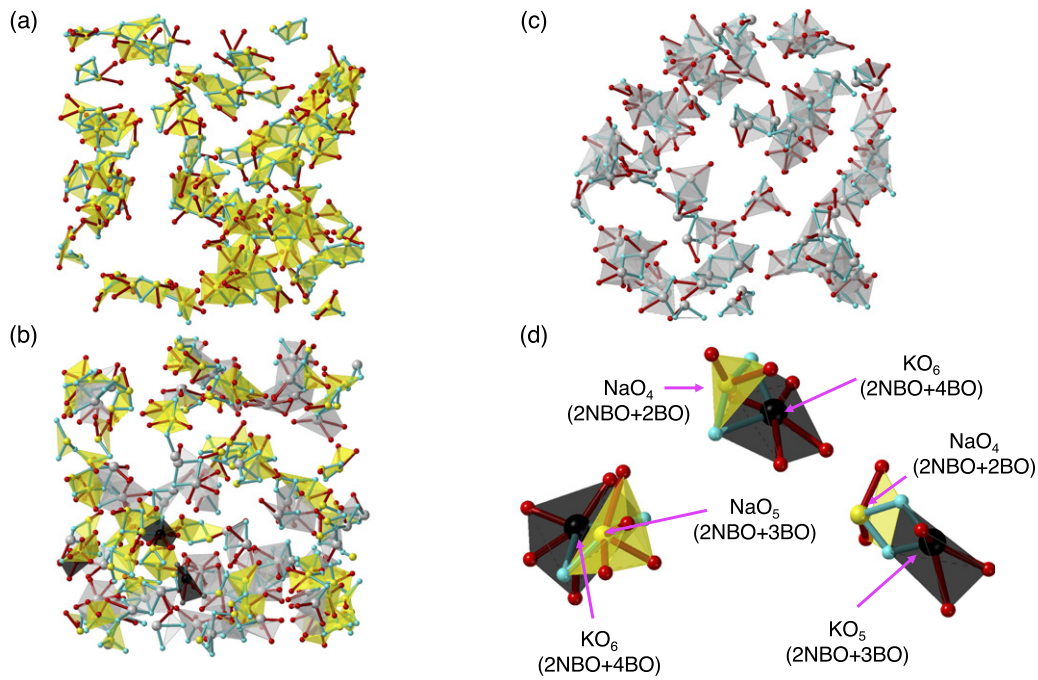


**Figure 16.** Visualization of alkali–oxygen polyhedra around NBO atoms in the  $22.7R_2O-77.3SiO_2$  glasses. Reproduced from [48]. **CC BY 4.0.** (a) Na100 glass, (b) Na50K50 glass, (c) K100 glass, and (d) typical bottleneck structures consisting of Na–O and K–O polyhedra. Red: BO; cyan: NBO; yellow: Na; grey: K. Alkali–oxygen polyhedra with edge-sharing of NBO atoms are visualized. Typical K–O polyhedra with increased BO coordination are highlighted in black.

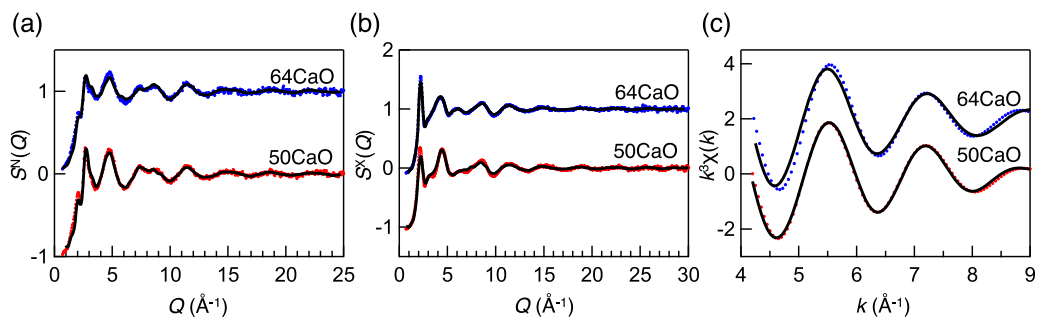


**Figure 17.** Neutron (a) and x-ray (b) total structure factors,  $S(Q)$  and EXAFS  $k^3\chi(k)$  (c) data for 50CaO and 64CaO glasses. The EXAFS  $k^3\chi(k)$  data were obtained by back-Fourier transform of the first correlation peak in  $|FT|$ . Circles: experimental data; curve: RMC–DFT model [58].

with increasing  $K_2O$  content. This ratio cannot provide any evidence of the mixed alkali effect in the intermediate-range structure, similarly to NMR data [100].

To shed light on the mixed alkali effect, the cavity volume distribution was calculated (figure 14(b)). The volume of the largest cavity in  $SiO_2$  glass is  $14\,206\text{ \AA}^3$ , and the maximum cavity volumes for the Na100, Na50K50, and K100 glasses are 166, 323, and  $1310\text{ \AA}^3$ , respectively, representing the nonlinear variation of the structure with increasing  $K_2O$  content. Indeed, figure 14(b) demonstrates that the maximum cavity size in the Na50K50 glass is clearly smaller than the average value of the Na100 and K100 glasses. Assuming that the size difference between sodium and potassium ions is  $0.4\text{ \AA}$ , the smaller size cavities should prevent the migration of potassium ions in the Na50K50 glass, which provides insight to discuss the mixed alkali effect.

To obtain more detailed information and reconcile the mixed alkali effect, we applied a novel topological approach, the persistent homology analysis. The alkali-centric PDs of Na50K50 glass for Na-centric, Na/K-centric, and K-centric data, shown in figure 15, reveal striking differences. None of the Na-centric (figure 15(a)) or K-centric (figure 15(c)) data has any characteristic profile, while the Na/K-centric PD (figure 15(b)) has two profiles at  $d_k \sim 5$  and  $\sim 10\text{ \AA}^2$ . These profiles demonstrate that Na and K are highly correlated with edge-sharing oxygens in Na50K50 glass, similar to a Na–O–K pattern. Indeed, a connectivity analysis [101] confirmed that 81% of Na, K, and O atoms form a network in Na50K50 glass.

The profiles shown in figures 15(d)–(f) are compared with the partial PDFs,  $g_{ij}(r)$ , for the series of alkali silicate glasses in figure 15(g). As seen in figure 15(g) (left), differences are

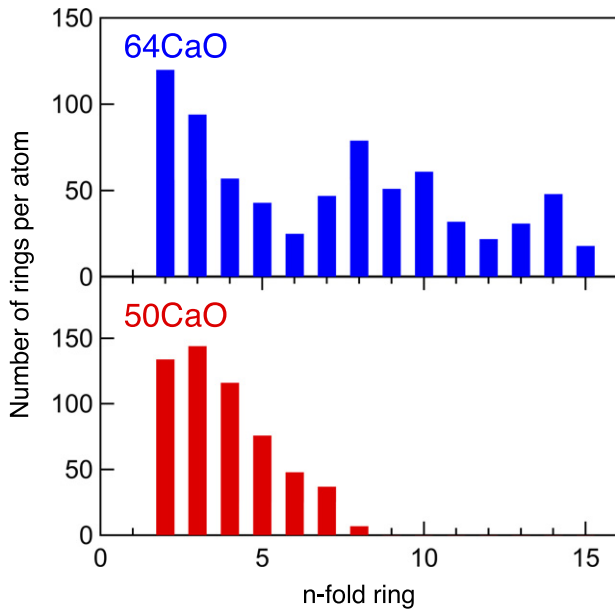


**Figure 18.** Distribution of Al(Ca)–O–Al(Ca)–O–Al(Ca) rings in 50CaO and 64CaO glasses obtained by RMC–DFT simulation [58].

negligible between  $g_{\text{NaNa}}(r)$ ,  $g_{\text{NaK}}(r)$ , and  $g_{\text{KK}}(r)$  because these functions contain only one-dimensional information. On the other hand, three-body correlations as a function of distance in figure 15(g) (right) show the formation of specific correlations between Na and K ions, as mentioned above. Thus, the PD enables us to extract the characteristic topology in these glasses.

To obtain more detailed structural information associated with the breakdown of the silicate network, alkali–oxygen polyhedra, with the formation of edge-sharing non-bridging oxygen (NBO) atoms in alkali silicate glasses, are visualized in figures 16(a)–(c). We believe that the visualization should provide us with crucial information for uncovering the origin of the mixed alkali effect. Unlike similar schematic drawings in the previous studies [98, 102, 103], we depicted atomistic configurations from the structural models that are consistent with both NMR and diffraction data. A comparison between the Na100 and K100 glasses suggests that the shape of the Na–O polyhedra is planar, whereas that of the K–O polyhedra is truly three-dimensional.

To understand the nature of alkali–oxygen polyhedra, we calculated the numbers of bridging oxygen (BO) and NBO atoms around the alkali ions. The alkali–NBO coordination number is  $\sim 2$  in both the Na100 and K100 glasses, and the alkali–BO coordination number is 2.1 in the Na100 glass. On the other hand, the K–BO coordination number in the K100 glass is 2.4, and this trend is enhanced in the Na50K50 glass, in which the K–BO coordination number is almost 3. The K–O polyhedra that are highly coordinated to the BO and Na–O polyhedra are highlighted in black in figure 16(b), where the potassium atom is trapped by a higher number of BO atoms (see figure 16(d)). It is likely that these specific configurations involving NBO atoms are a bottleneck for ionic conduction because the trapped potassium ions disturb ionic migration.

On the basis of the results of MD simulations of lithium potassium metasilicate glasses, it has been reported that each kind of alkali ion has an independent conduction pathway [104]. Accordingly, Habasaki *et al* found that the transfer of alkali ions through different ionic sites has a low probability and proposed an interpretation with restricted ion jumping between sites occupied by different types of ions. This seemed to be necessary owing to a mismatch between occupation energies of unlike alkali ions [105]. This intriguing finding that the local environment of potassium ions in highly coordinated K–O polyhedra is significantly different from that of sodium ions in the four-coordinated Na–O polyhedra successfully proved their hypothesis. In addition, specific correlations between the different ions that are found in the Na50K50 glass by persistent homology (figure 15(g) (right)) and connectivity analyses profoundly inhibited ionic migration in the Na50K50 glass. Hence, the local structure associated with alkali connectivity is the intrinsic origin of the mixed alkali effect, which supports the MRN model proposed by Greaves with a bottleneck structure [98].

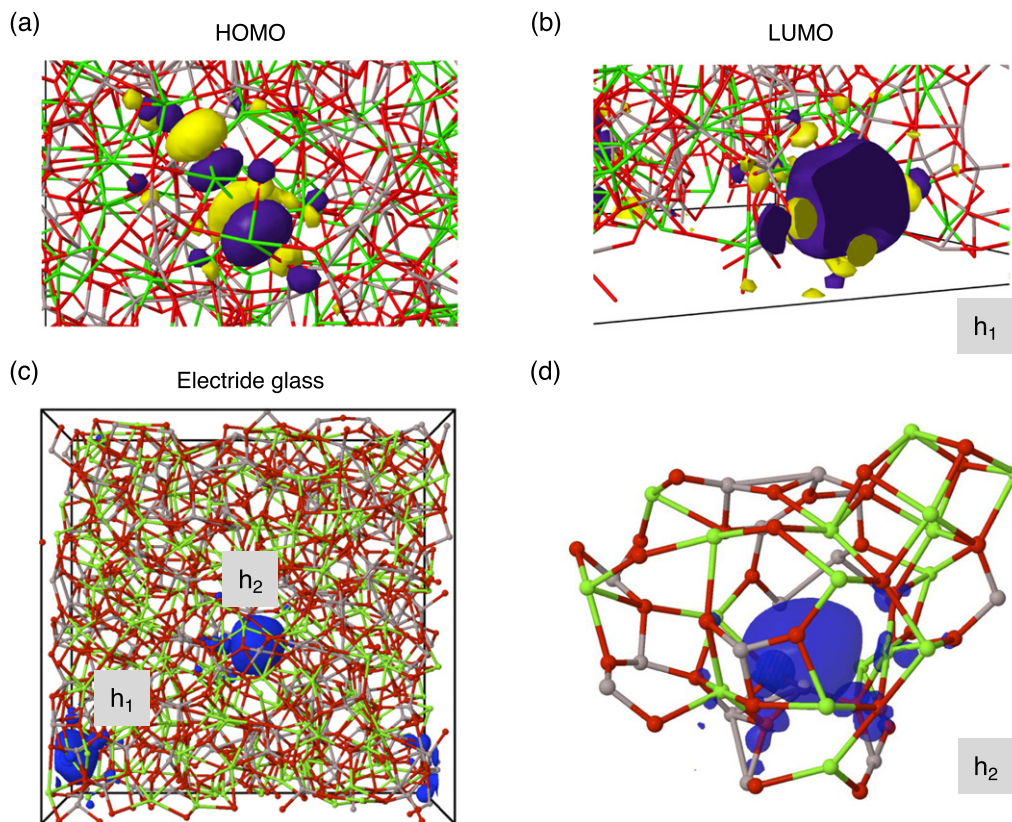
### 3.3. CaO–Al<sub>2</sub>O<sub>3</sub> glass

Glass formation in the CaO–Al<sub>2</sub>O<sub>3</sub> system is an important phenomenon because the glass system does not contain a typical network former. The RMC modelling was combined with density functional theory (DFT) simulations to investigate the relationship between the atomistic/electronic structures and the glass forming ability (GFA) in the 50CaO–50Al<sub>2</sub>O<sub>3</sub> (50CaO) and the 64CaO–36Al<sub>2</sub>O<sub>3</sub> (64CaO) glasses. These compositions were chosen because the GFA of the 50CaO glass is much lower than that of the 64CaO glass, although the composition difference is very small.

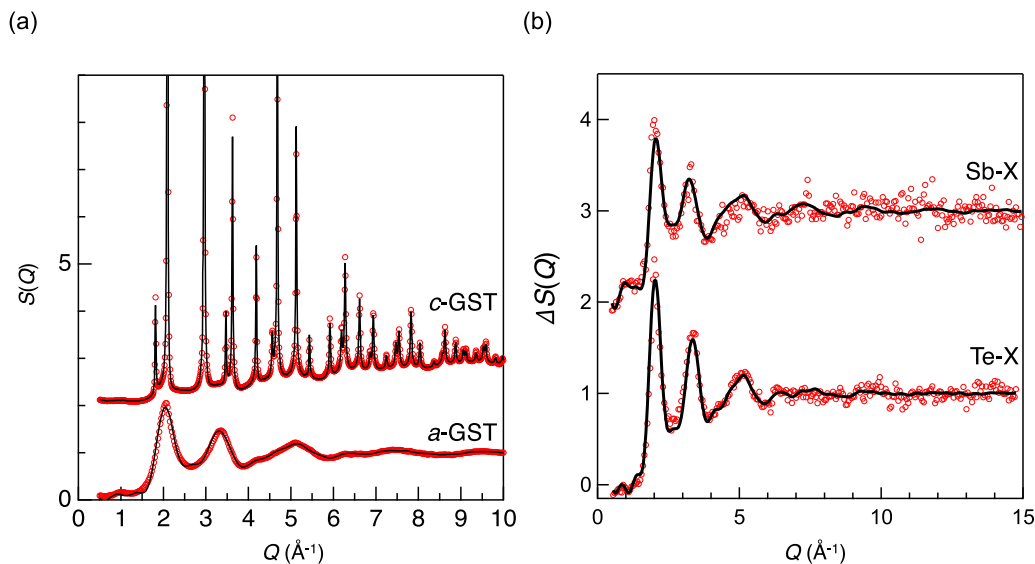
Figures 17(a)–(c) show neutron and x-ray total structure factors,  $S^{\text{N,X}}(Q)$  [58], and Ca K edge EXAFS  $k^3\chi(k)$  data, respectively, of 50CaO and 64CaO glasses as coloured dots, together with the results of RMC–DFT simulations (black curves). Differences in diffraction and EXAFS data are very small between the two compositions, suggesting that the short-range structure is similar in the two glasses. Both the neutron and x-ray total structure factors,  $S^{\text{N,X}}(Q)$ , show an FSDP at  $Q \sim 2.2 \text{ \AA}^{-1}$ , but the x-ray data show a sharper peak, because x-rays are more sensitive to the cation–cation correlation than neutrons. Moreover, the FSDP for the 64CaO glass is higher than that for the 50CaO glass in the x-ray data. The partial PDFs,  $g_{ij}(r)$ , of the CaO–Al<sub>2</sub>O<sub>3</sub> glasses obtained by RMC–DFT simulation show very small differences between the 50CaO glass and 64CaO glass. The Al–O coordination number,  $N_{\text{Al-O}}$ , is 4.26 for the 50CaO glass and 4.14 for the 64CaO glass. The Ca–O coordination number,  $N_{\text{Ca-O}}$ , is 5.02 for the 50CaO glass and 4.92 for the 64CaO glass.

Figure 18 shows the distributions of –Al(Ca)–O–Al(Ca)–O–Al(Ca)– rings in CaO–Al<sub>2</sub>O<sub>3</sub> glasses. The 50CaO glass (low GFA) has a very narrow ring-size distribution, whereas the 64CaO glass (high GFA) has a wide ring size distribution. This trend can be understood on the basis of the concept





**Figure 19.** Close-up visualizations of (a) HOMO and (b) LUMO single-particle electron states in the 64CaO glass.  $h_1$  indicates the cavity (cage) occupied by the LUMO. Yellow and magenta represent the different signs of the wave-function nodes. (c) Simulation box and the electron spin density of the 64CaO glass with one oxygen removed at  $h_2$ , i.e., with two additional electrons. (d) Cage structure around the spin density of one electron corresponding to the  $h_2$  cavity (close-up of (c)). Al: grey; Ca: green; O: red [58].



**Figure 20.** Experimental data (open circles) and the results of RMC modelling (solid curve). (a) X-ray total structure factors,  $S(Q)$  for c-GST and a-GST. (b) Differential structure factors,  $\Delta S(Q)$ , for a-GST measured at Sb and Te K absorption edges. [65] John Wiley & Sons. Copyright © 2012 WILEY-VCH Verlag GmbH & Co. KGaA, Weinheim.  $S(Q)$  for c-GST and  $\Delta S(Q)$  for Sb are shifted upward by two units for clarity. X: Ge, Sb, Te.

of topological order–disorder according to Gupta and Cooper [45]. This characteristic ring-size distribution, and particularly the formation of large rings in the 64CaO glass, indicates the

existence of a cage structure [106] at the eutectic composition. In addition, it is suggested that the topological disorder in the 64CaO glass is a signature of a stronger liquid [94] than the

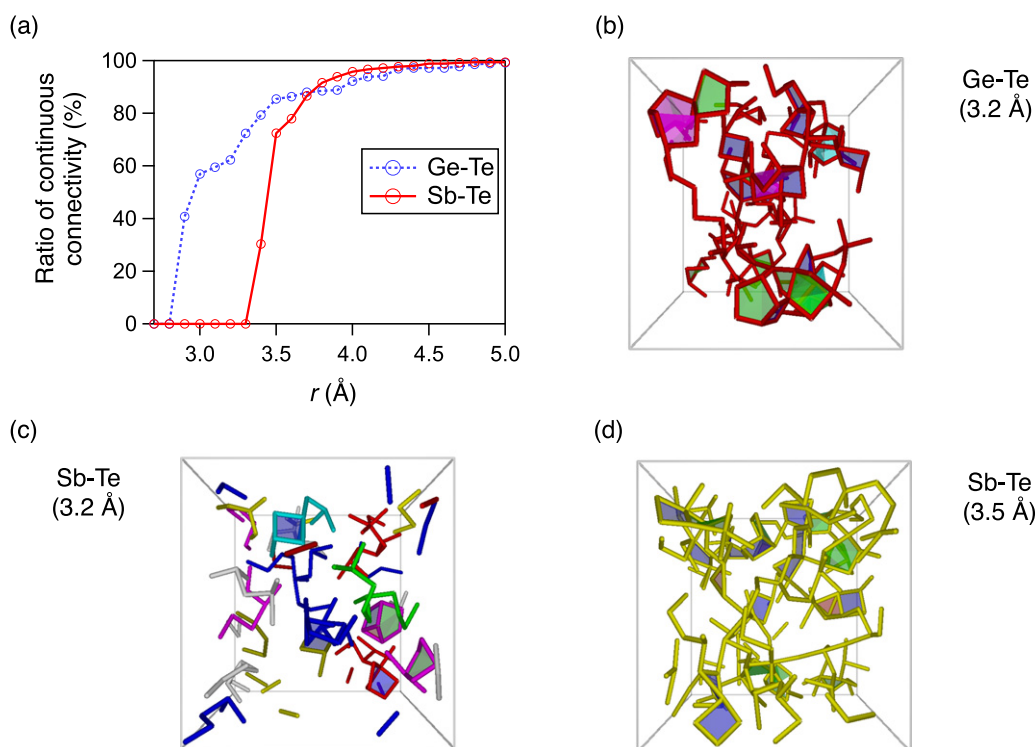


**Figure 21.** RMC-generated atomic configurations and connectivity of GeTe and SbTe in a-GST. [65] John Wiley & Sons. Copyright © 2012 WILEY-VCH Verlag GmbH & Co. KGaA, Weinheim. (a) Connectivity of GeTe and SbTe for different values of  $r_{\max}$ . (b) Atomic configuration of GeTe (connectivity of GeTe for  $r_{\max} = 3.2$  Å). (c) Atomic configuration of SbTe (connectivity of SbTe for  $r_{\max} = 3.2$  Å). (d) Atomic configuration of SbTe (connectivity of SbTe for  $r_{\max} = 3.5$  Å). The threefold, fourfold, fivefold, and sixfold rings are highlighted by red, blue, green, and light blue colours, respectively.

50CaO glass. This scenario can reasonably explain the high GFA of the 64CaO glass without the need for the presence of a traditional network former, as proposed in Zachariassen's original theory [75].

The synthesis of 'C12A7' (63.2CaO–36.8Al<sub>2</sub>O<sub>3</sub>): e<sup>-</sup> electride glass from a strongly reduced high-temperature melt has been performed by Kim *et al* [106]. It is assumed that the removal of excess O atoms from AlO<sub>5</sub> and AlO<sub>6</sub> units in the C12A7 melt results in the formation of cage structures in the electride glass, which can host solvated electrons. To shed light on the early stage of the formation of the electride glass, the highest occupied molecular orbital (HOMO) and lowest unoccupied molecular orbital (LUMO) single-particle states of electrons were computed for the 64CaO glass by DFT simulation, as illustrated in figures 19(a) and (b). The characteristics of the HOMO and LUMO states are different: while the former is located across atoms and bonds (figure 19(a)), the latter is associated with a cavity, forming a spin-paired state analogous to an F-center in a vacancy site of crystalline MgO (h<sub>1</sub> in figure 19(b)). The calculated HOMO–LUMO gap is 1.71 eV.

Since it is well known that DFT simulations at this level underestimate band gaps by approximately a factor of two, this value is consistent with the typical insulating electronic behaviour and transparent properties of the 64CaO glass. Furthermore, the RMC-DFT model suggests that the first three cage-trapped LUMO states appear as impurity states below the onset of the conduction band. Following the idea of bipolaron

states and a conducting electride glass, we removed one oxygen atom from the h<sub>2</sub> site in figure 19(c), thus releasing two additional electrons from the cations while keeping the total charge neutral; then the structure was optimized for several spin configurations by DFT. In the spin-degenerate case, where there is no distinction concerning the 'spin' of electrons, these electrons occupy the cavity vacated by the removed oxygen (marked as h<sub>2</sub> in figure 19(c)), yielding a HOMO state similar to that of the LUMO state of the parent system. On the other hand, the removal of the spin degeneracy (triplet spin configuration) leads to a 0.97 eV more energetically stable electronic configuration, where the two additional electrons have the same spin and are located in well-separated cavities (figure 19(c), h<sub>1</sub> and h<sub>2</sub>). This procedure was repeated for two, three, and four removed oxygen atoms (four, six, and eight additional electrons), and in all cases, the separated (solvated) electrons in individual cages were energetically more favorable than the F-center-like states (two electrons exist in one cavity). An example of the cage structure around a single electron (spin density) is presented in figure 19(d). These cases confirm that by removing oxygen from the standard stoichiometry, one can achieve local spin states in the 64CaO glass. Furthermore, the gradual removal of O increases the number of impurity states within the electronic band gap, leading to changes in conductivity owing to a narrower band gap. Although this is a simulation of a very early stage in the formation of electride glass, it is suggested that the combination of RMC modelling and DFT simulation is a powerful tool

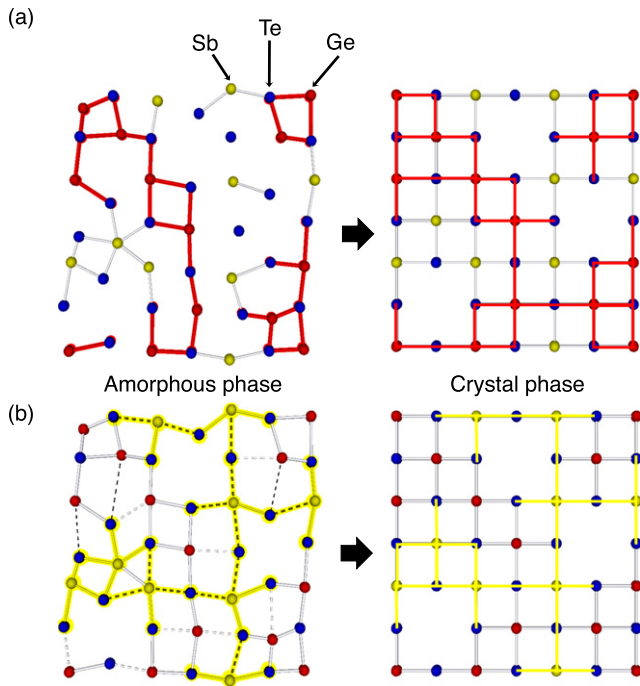


**Figure 22.** Schematic drawing of phase-change process in a-GST: (a) highlights the Ge–Te network and (b) highlights the Sb–Te pseudonetwork. The sticks represent GeTe (red) and SbTe (yellow) bonds up to 3.2 Å, and the dotted yellow lines show SbTe correlations of 3.2–3.5 Å in the amorphous phase. [65] John Wiley & Sons. Copyright © 2012 WILEY-VCH Verlag GmbH & Co. KGaA, Weinheim.

for understanding the glassy structure at both the atomic and electronic levels.

### 3.4. Fast phase-change materials

Although data storage and distribution via the internet is dominant nowadays, digital versatile disk (DVD)/Blu-ray (BD) systems are still important media in our daily lives. Information is stored on a DVD/BD in the form of microscopic bits in a thin layer of polycrystalline  $\text{Ge}_2\text{Sb}_2\text{Te}_5$  (GST). The bits can have a disordered, amorphous structure (recorded) or an ordered, crystalline structure (erased). The phase change between the two phases lasts only a few tens of nanoseconds upon laser irradiation [107]. The use of the combination of synchrotron hard XRD, AXS measurements, and DF–MD/RMC modelling on GST has enabled us to determine the structures of both phases and made it possible to generate a model to explain not only the fast phase change and its high durability, but also, in particular, the stability of the amorphous phase at room temperature.

Figure 20(a) shows the x-ray total structure factors  $S(Q)$  for crystalline (c)-GST and amorphous (a)-GST [65].  $S(Q)$  of c-GST shows sharp Bragg peaks with a diffuse scattering pattern, while only the latter appears for a-GST. It was confirmed that  $S(Q)$  from the RMC model (solid curve) is in excellent agreement with experimental data (open circles). The differential structure factors  $\Delta S(Q)$  of a-GST at the Sb and Te K edges, obtained from AXS measurements, are shown in figure 20(b). Although the statistics is not very good, we can observe

distinct differences between the Sb- and Te-related data at  $Q < 6 \text{ \AA}^{-1}$ , suggesting that AXS can distinguish Sb (atomic number of 51)-related and Te (atomic number of 52)-related correlations beyond the nearest-neighbor distance. The differential structure factor of Sb,  $\Delta S_{\text{Sb}}(Q)$ , exhibits an FSDP at  $Q \sim 1 \text{ \AA}^{-1}$ , which is also observed in the x-ray  $S(Q)$  data for both the amorphous and crystalline phases, as shown in figure 20(a), although the FSDP is not prominent in comparison with that of a typical glass-forming material such as  $\text{SiO}_2$  glass.

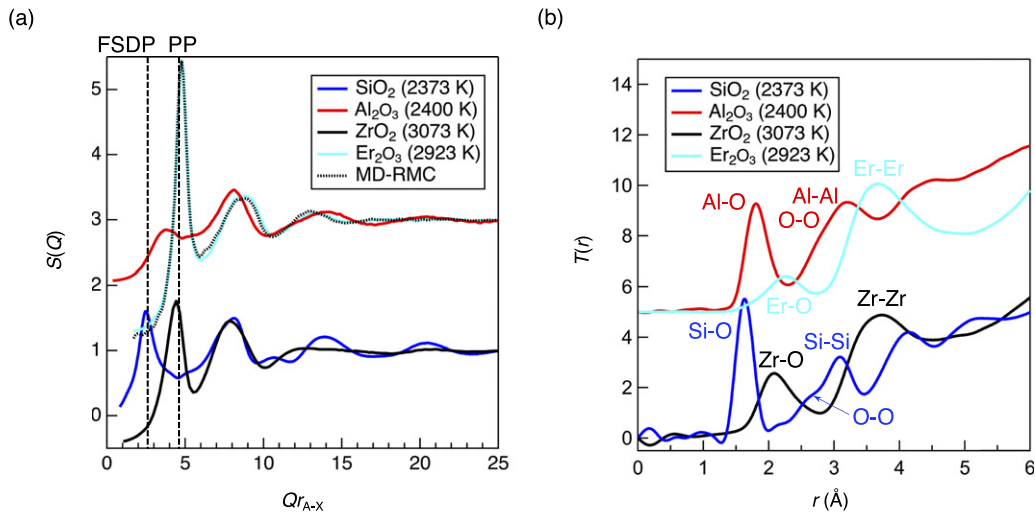
To investigate the atomistic ordering induced by Ge–Te and Sb–Te bonds in detail, connectivities between atoms were calculated for various maximum distances ( $r_{\text{max}}$ ) within which atomic pairs were considered to be connected. As can be seen in figure 21(a), almost 60% of the Ge–Te bonds form a continuous network when  $r_{\text{max}}$  is 3.2 Å, while Sb–Te bonds do not form a network. This distance corresponds to the bond length determined by DF–MD simulation [108]. Atomic configurations of Ge–Te and Sb–Te with bonds considered up to a distance of 3.2 Å are shown in figures 21(b) and (c), respectively. It is observed that Ge–Te bonds form a continuous network, that stabilizes the amorphous phase, whereas Sb–Te bonds do not. Moreover, Ge–Te bonds form large fractions of fourfold (highlighted in blue) and sixfold (highlighted in light blue) rings. On the other hand, about 70% of the Sb–Te pairs form a pseudonetwork, as can be seen in figures 21(a) and (d), when  $r_{\text{max}}$  is 3.5 Å. In other words, the Sb–Te pseudonetwork becomes visible when the correlation distance is increased to 3.5 Å, whereas such a feature cannot be observed for Ge–Te connectivity.

Figure 22 illustrates the fast phase-change process based on the structural features in a-GST. As highlighted in red in the figure, Ge–Te bonds contribute to the formation of a network composed of fourfold rings. Therefore, Ge and Te can be recognized as network-forming elements that ensure the long-term stability of the amorphous phase. The Ge–Te network may remain in the crystalline phase, which explains the fast crystallization. As highlighted in yellow in figure 22, the Sb–Te correlations beyond the nearest coordination distance can form a Sb–Te pseudonetwork. This unusual atomic ordering in Sb–Te correlations is ascribed to the combination of two positively charged atoms (Ge, 0.22 electrons; Sb, 0.32 electrons; Te, 0.22 electrons [108]) that allow critical nuclei to form in the amorphous phase via the formation of Sb–Te bonds through small atomic displacements of antimony and tellurium atoms.

### 3.5. Liquid $\text{Er}_2\text{O}_3$

Determining the liquid structure is the first step in understanding the nature of glass–liquid transitions. However, a diffraction measurement of liquid provides very limited structural information because the liquid structure lacks long-range periodicity, and a Fourier transform of the diffraction data provides only pairwise correlations. Moreover, high-quality measurements are difficult to obtain at high temperatures.

$\text{Er}_2\text{O}_3$  is a representative nonglass former that is commonly used as a refractory material and dopant for



**Figure 23.** (a) Faber–Ziman x-ray total structure factors,  $S(Q)$ , for  $l\text{-Er}_2\text{O}_3$  [reproduced from [71]. CC BY 4.0],  $l\text{-SiO}_2$  [116],  $l\text{-Al}_2\text{O}_3$  [reprinted (figure) with permission from [69], Copyright (2013) by the American Physical Society], and  $l\text{-ZrO}_2$  [70] together with that of  $l\text{-Er}_2\text{O}_3$  derived from the MD–RMC simulation [66]. The  $l\text{-Er}_2\text{O}_3$  and  $l\text{-Al}_2\text{O}_3$  data are displaced upward by 2 for clarity. (b) Total correlation functions  $T(r)$ , for  $l\text{-Er}_2\text{O}_3$  [reproduced from [71]. CC BY 4.0],  $l\text{-SiO}_2$  [116],  $l\text{-Al}_2\text{O}_3$  [Reprinted (figure) with permission from [69], Copyright (2013) by the American Physical Society], and  $l\text{-ZrO}_2$  [reproduced from [70]. CC BY 4.0]. The  $l\text{-Er}_2\text{O}_3$  and  $l\text{-Al}_2\text{O}_3$  data are displaced upward by 5 for clarity.

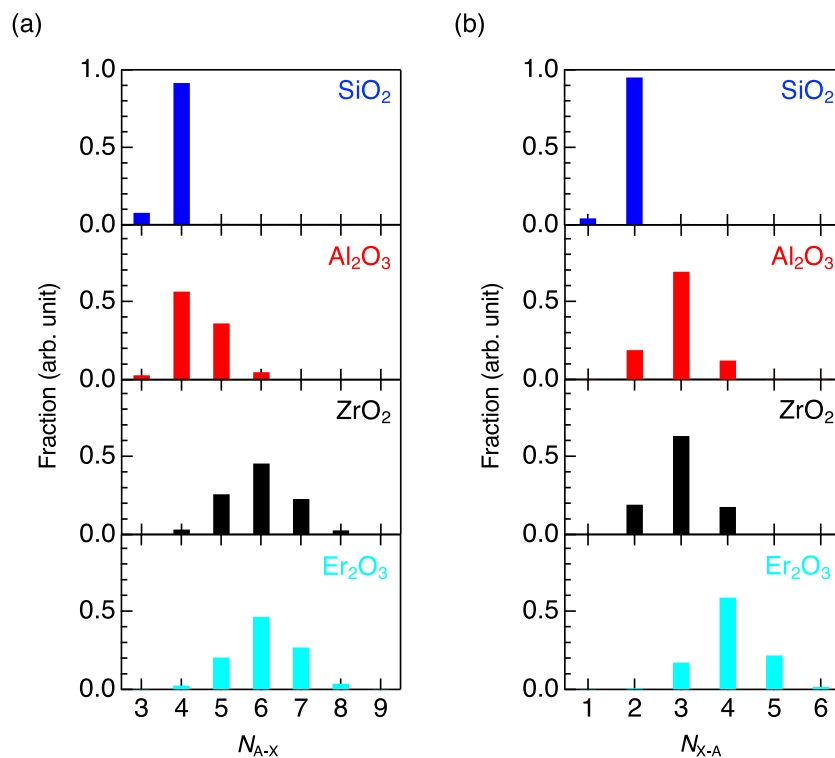


**Figure 24.** Coordination number distributions in  $l\text{-Er}_2\text{O}_3$  [reproduced from [71]. CC BY 4.0],  $l\text{-SiO}_2$  [116],  $l\text{-Al}_2\text{O}_3$  [reprinted (figure) with permission from [69], Copyright (2013) by the American Physical Society], and  $l\text{-ZrO}_2$  [reproduced from [70]. CC BY 4.0]. (a)  $N_{A-X}$ , (b)  $N_{X-A}$ .

luminescent materials. Because  $\text{Er}_2\text{O}_3$  has an extremely high melting point ( $T_m = 2686$  K), the difficulties in handling the liquid lead to problems in selecting suitable container materials that do not contaminate the sample. To avoid contact with other materials, levitation furnaces that enable us to measure precise synchrotron XRD and thermophysical properties for

liquids at extremely high temperatures [29, 109–111] have been developed.

In this section, we present the results of accurate hard XRD and density measurements on containerless levitated  $l\text{-Er}_2\text{O}_3$  using an electrostatic levitation furnace (ELF) at the International Space Station (ISS) [112] as it is impossible



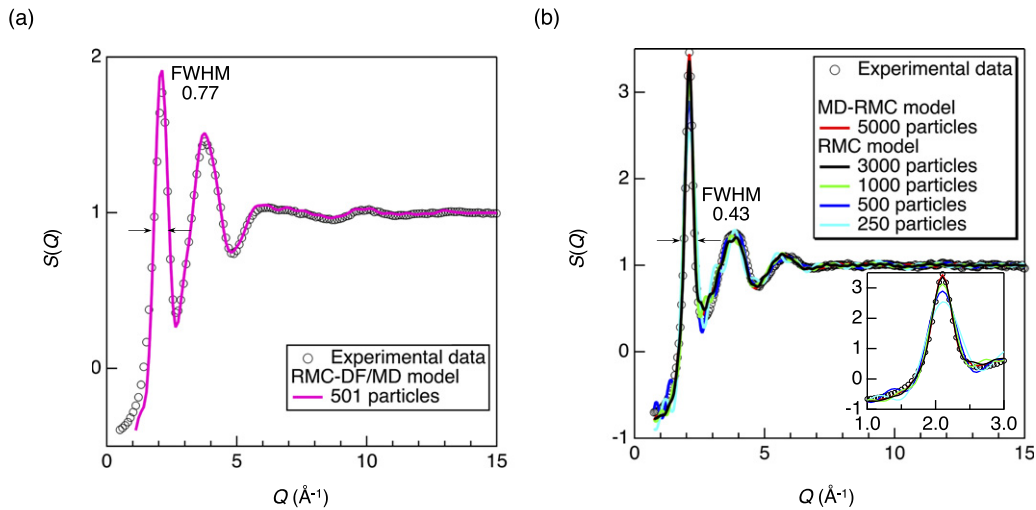


**Figure 25.** X-ray total structure factors,  $S(Q)$ , obtained from hard XRD measurements and simulations. (a)  $l$ -ZrO<sub>2</sub> [reproduced from [70]. CC BY 4.0], (b)  $l$ -Er<sub>2</sub>O<sub>3</sub> [reproduced from [71]. CC BY 4.0]. The inset shows an enlarged principal peak.

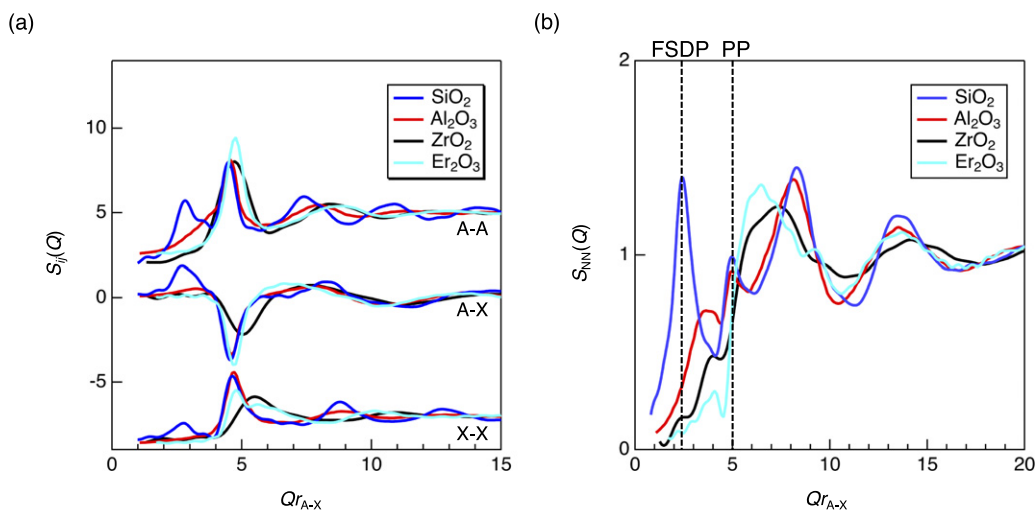


**Figure 26.** Partial structure factors for  $l$ -Er<sub>2</sub>O<sub>3</sub> [reproduced from [71]. CC BY 4.0],  $l$ -SiO<sub>2</sub> [116],  $l$ -Al<sub>2</sub>O<sub>3</sub> [reprinted (figure) with permission from [69], Copyright (2013) by the American Physical Society], and  $l$ -ZrO<sub>2</sub> [reproduced from [70]. CC BY 4.0]. (a) Faber–Ziman partial structure factors. (b) Bhatia–Thornton number–number partial structure factors  $S_{NN}(Q)$ . The scattering vector  $Q$  is scaled by multiplying by  $r_{A-X}$  (distance between the centre and corner of the polyhedron).

to measure density data on the ground. We also performed MD–RMC simulations and obtained PDs from topological analyses to demonstrate liquid properties at the atomic level, comparing  $l$ -Er<sub>2</sub>O<sub>3</sub> with other non-GFLs and a typical GFL,  $l$ -SiO<sub>2</sub>. The combination of an experiment and a simulation allows trends in single-component nonglass-forming liquid oxides to be identified, with a focus on atomic ordering and topology. Furthermore, we compared the features of single-component nonglass-forming oxide liquids with those of other systems.

The Faber–Ziman total structure factors,  $S(Q)$ , for  $l$ -Er<sub>2</sub>O<sub>3</sub> [71],  $l$ -SiO<sub>2</sub> [89],  $l$ -Al<sub>2</sub>O<sub>3</sub> [69], and  $l$ -ZrO<sub>2</sub> [70], together with the results of the MD–RMC simulation for  $l$ -Er<sub>2</sub>O<sub>3</sub>, are compared in figure 23(a). Note that the scattering vector  $Q$  is scaled by multiplying by  $r_{A-X}$  (distance between the centre and corners of the polyhedron). The experimental  $S(Q)$  of  $l$ -Er<sub>2</sub>O<sub>3</sub>

(solid cyan curve) is well reproduced by the MD–RMC simulation (dotted black curve) using the liquid density measured by the ISS-ELF. A well-defined FSDP [78] is observed only for  $l$ -SiO<sub>2</sub> (GFL) at  $Qr_{A-X} = 2.6$ , while a PP [78] is observed in both the  $l$ -ZrO<sub>2</sub> and  $l$ -Er<sub>2</sub>O<sub>3</sub> data at  $Qr_{A-X} \sim 4.5$ . On the other hand,  $l$ -Al<sub>2</sub>O<sub>3</sub> gives rise to a small peak between the FSDP and PP, suggesting that the structure of  $l$ -Al<sub>2</sub>O<sub>3</sub> is intermediate [69] between those of  $l$ -SiO<sub>2</sub> and  $l$ -ZrO<sub>2</sub>/ $l$ -Er<sub>2</sub>O<sub>3</sub>. It is well known that the PP reflects the packing of oxygen atoms in ND data [113], since neutrons are sensitive to oxygen. For the same reason, a PP is not observed in the x-ray  $S(Q)$  for  $l$ -SiO<sub>2</sub> (see figure 23(a)), and the origin of the PP in  $l$ -ZrO<sub>2</sub> and  $l$ -Er<sub>2</sub>O<sub>3</sub> is ascribed to the packing of cations. The x-ray total correlation functions  $T(r)$  for  $l$ -Er<sub>2</sub>O<sub>3</sub> [71],  $l$ -SiO<sub>2</sub> [89],  $l$ -Al<sub>2</sub>O<sub>3</sub> [69], and  $l$ -ZrO<sub>2</sub> [70] are shown in figure 23(b). The first peak observed at approximately 2.2 Å is assigned to the

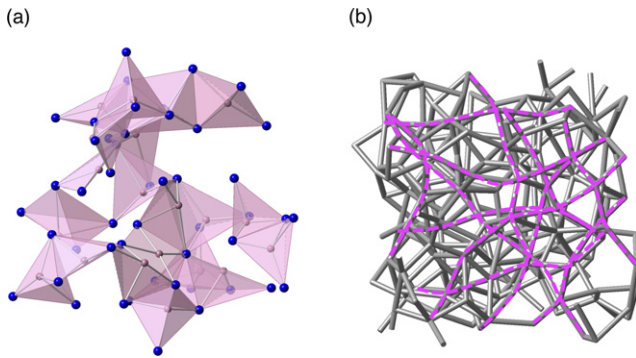


**Figure 27.** (a) Visualization of the  $\text{OEr}_4$  tetracluster network in  $l\text{-Er}_2\text{O}_3$ . Pink: oxygen; blue: erbium. (b) Visualization of the nearly linear arrangements of  $\text{Er-O-Er}$ . Reproduced from [71]. CC BY 4.0.

$\text{Er-O}$  correlation, and a tail to  $\sim 3 \text{ \AA}$  implies the formation of distorted  $\text{ErO}_n$  polyhedra in the liquid. The second peak, observed at  $3.7 \text{ \AA}$ , can be assigned mainly to the  $\text{Er-Er}$  correlation, and the  $\text{O-O}$  correlation peak is unclear owing to its small weighting factor for x-rays. The  $\text{Er-O}$  correlation length of  $2.2 \text{ \AA}$ , as well as that of  $\text{Zr-O}$  ( $2.1 \text{ \AA}$ ), is larger than those of  $\text{Si-O}$  ( $\sim 1.63 \text{ \AA}$  at  $2373 \text{ K}$ ) and  $\text{Al-O}$  ( $\sim 1.78 \text{ \AA}$  at  $2400 \text{ K}$ ) owing to substantial differences between the ionic radii of the elements. The increased cation-oxygen correlation length in the liquid phases of  $\text{Er-O}$  and  $\text{Zr-O}$  suggests that the oxygen coordination number around cations is higher than 4 because the  $\text{Er-O}$  correlation length ( $2.2 \text{ \AA}$ ) or  $\text{Zr-O}$  correlation length ( $2.1 \text{ \AA}$ ) is close to the sum of the ionic radii of oxygen ( $1.35 \text{ \AA}$ ) and sixfold erbium ( $0.89 \text{ \AA}$ ) or zirconium ( $0.72 \text{ \AA}$ ), respectively. These features indicate that the structures of  $l\text{-Er}_2\text{O}_3$  and  $l\text{-ZrO}_2$  are primarily ionic and close-packed, that consist of large interconnected polyhedral units. These units are very different from those found in  $l\text{-SiO}_2$  and  $l\text{-Al}_2\text{O}_3$ . This behaviour is consistent with the fact that the peaks observed at  $Qr_{\text{A-X}} \sim 4.5$  in figure 23(a) are not the FSDP, which is typically associated with IRO in oxide glasses and the liquids; thus, there is no such ordering in  $l\text{-Er}_2\text{O}_3$  and  $l\text{-ZrO}_2$  because of the very densely packed structure. The coordination number distributions,  $N_{\text{A-X}}$  and  $N_{\text{X-A}}$ , for  $l\text{-Er}_2\text{O}_3$  [71],  $l\text{-SiO}_2$  [89],  $l\text{-Al}_2\text{O}_3$  [69], and  $l\text{-ZrO}_2$  [70] obtained from the simulation are compared in figures 24(a) and (b). The  $\text{Er-O}$  coordination number (up to  $3.0 \text{ \AA}$ ) is found to be 6.1 from our combined MD-RMC simulation, which is rather close to the crystalline phase [114], and the  $\text{O-Er}$  coordination number can be estimated to be 4.1. These results suggest that cations are tetrahedrally coordinated in  $l\text{-SiO}_2$  (GFL), while they are octahedrally coordinated in  $l\text{-ZrO}_2$  and  $l\text{-Er}_2\text{O}_3$  (non-GFLs), and the cation-oxygen coordination number in  $l\text{-Al}_2\text{O}_3$  is intermediate [69] between those of GFL and  $l\text{-ZrO}_2/l\text{-Er}_2\text{O}_3$ , although  $l\text{-Al}_2\text{O}_3$  is a non-GFL. This behaviour is consistent with that of the first correlation peaks in experimental real-space functions (see figure 23(b)) and with the fact that the viscosity of  $l\text{-ZrO}_2$  is approximately one-tenth of that in  $l\text{-Al}_2\text{O}_3$  [70]. Another interesting behaviour is observed for the oxygen-cation coordination numbers. It is demonstrated that oxygen is twofold in  $l\text{-SiO}_2$ , which is a signature of the formation of a sparse

network, while triclusters ( $\text{XA}_3$ ) are dominant in  $l\text{-Al}_2\text{O}_3$  and  $l\text{-ZrO}_2$ . The formation of tetraclusters ( $\text{XA}_4$ ) is confirmed in  $l\text{-Er}_2\text{O}_3$ , suggesting that this behaviour is a distinct feature of this liquid. Moreover, it is implied that the behaviour of the coordination numbers in a series of oxide liquids is affected by both the composition and the ionic radii between the constituent anions and cations. For instance, the ionic radii of Si and Al are small, which results in tetrahedral coordination, although the  $\text{Al-O}$  coordination number is greater than four on average. The tetracluster formation is governed by the ratio of Er and O in  $\text{Er}_2\text{O}_3$ .

As shown in figure 23(a), the PP of  $l\text{-Er}_2\text{O}_3$  is very sharp compared with that of  $l\text{-ZrO}_2$ . The FWHM of the PP in  $l\text{-Er}_2\text{O}_3$  is 0.43, in comparison with 0.77 in  $l\text{-ZrO}_2$  (see figure 25). A simulation box with 501 particles was used in the previous RMC-DF simulation for  $l\text{-ZrO}_2$  [70], where a good agreement was observed between the experimental and simulated data (see figure 25(a)). However, as can be seen in the inset data of figure 25(b), a simulation box of 500 particles is insufficient to reproduce the sharp PP in  $l\text{-Er}_2\text{O}_3$ ; larger atomic models are needed to reproduce this feature. Insight into the structure of  $l\text{-Er}_2\text{O}_3$ , in comparison with those of  $l\text{-SiO}_2$  and other non-GFLs, can be obtained by calculating the Faber-Ziman partial structure factors,  $S_{ij}(Q)$ , and the Bhatia-Thornton [115] number-number partial structure factor,  $S_{\text{NN}}(Q)$ , which indicates the topological order in a system; where  $S_{ij}(Q)$  is a Faber-Ziman partial structure factor and  $c_i$  denotes the atomic fraction of chemical species  $i$ . Moreover, it is possible to compare data for the four liquids while ignoring the difference in the sensitivity of elements to x-rays because the weighting factors for x-rays are eliminated in  $S_{\text{NN}}(Q)$ . The  $S_{ij}(Q)$  values calculated from the simulation models for  $l\text{-Er}_2\text{O}_3$  [71],  $l\text{-SiO}_2$  [89],  $l\text{-Al}_2\text{O}_3$  [69], and  $l\text{-ZrO}_2$  [70] are shown in figure 26(a). It is confirmed that a very sharp PP in  $l\text{-Er}_2\text{O}_3$  can be assigned to the  $\text{Er-Er}$  correlation.  $S_{\text{NN}}(Q)$  for  $l\text{-Er}_2\text{O}_3$  and those for  $l\text{-SiO}_2$  and other non-GFLs are shown in figure 26(b). As mentioned above, only  $l\text{-SiO}_2$  exhibits an FSDP at  $Qr_{\text{A-X}} = 2.6$ . The  $Q_{\text{FSDP}}$  position arises from an underlying periodicity of  $2\pi/Q_{\text{FSDP}}$  that originates, for example, from the formation of pseudo-Bragg planes with a finite correlation length of  $2\pi/\Delta Q_{\text{FSDP}}$  in  $l\text{-SiO}_2$ , while neither  $l\text{-Al}_2\text{O}_3$ ,  $l\text{-ZrO}_2$ , nor  $l\text{-Er}_2\text{O}_3$  show an FSDP in  $S_{\text{NN}}(Q)$ , as discussed by Kohara *et al* [70]. Since the Bhatia-Thornton  $S_{\text{NN}}(Q)$  can eliminate the weighting factors for x-rays, the absence of an FSDP in  $S_{\text{NN}}(Q)$  is characteristic of a non-GFL. Another important feature in  $S_{\text{NN}}(Q)$  is that  $l\text{-SiO}_2$  and  $l\text{-Al}_2\text{O}_3$  exhibit a second PP at  $Qr_{\text{A-X}} \sim 5$ , while a PP is indistinct in the  $l\text{-ZrO}_2$  and  $l\text{-Er}_2\text{O}_3$  data.

The absence of an FSDP in the  $l\text{-ZrO}_2$  and  $l\text{-Er}_2\text{O}_3$  data suggests that both cations and oxygen are densely packed. This feature in  $l\text{-Er}_2\text{O}_3$  can be manifested by the formation of the  $\text{OEr}_4$  tetracluster network shown in figure 27(a). This network cannot be found in  $l\text{-Al}_2\text{O}_3$  or in  $l\text{-ZrO}_2$ , suggesting that the very sharp PP in  $l\text{-Er}_2\text{O}_3$  is a specific signature of the formation of a tetracluster network with long-range periodicity.

To reveal the origin of the very sharp PP in  $l\text{-Er}_2\text{O}_3$ , we calculated the bond angle distributions of the liquid and the

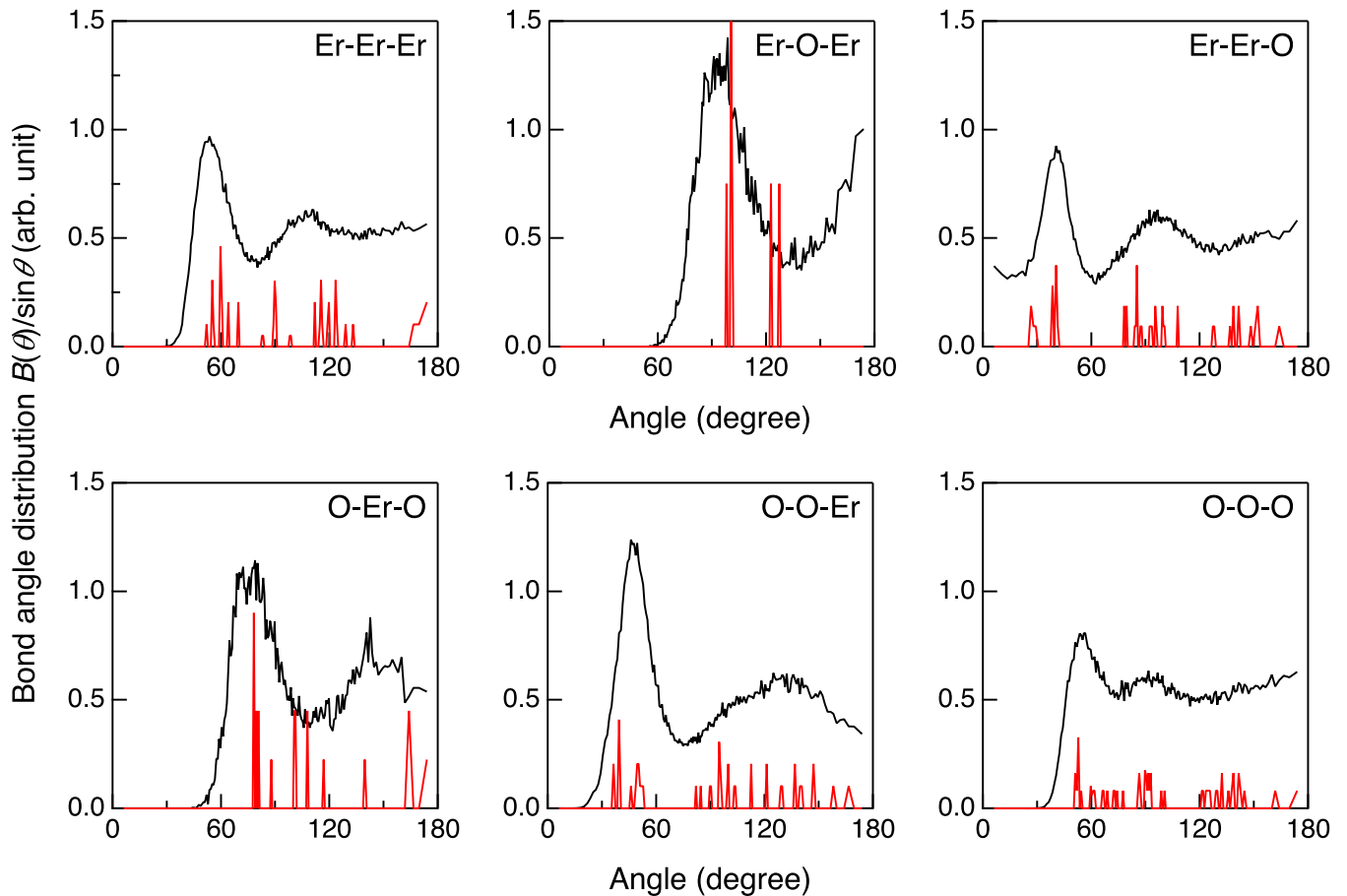


**Figure 28.** Bond angle distributions for  $\text{Er}_2\text{O}_3$ . Black line: liquid; red line: crystal. The  $B(\theta)/\sin\theta$  data for the crystalline data have been scaled by a factor of 20 for clarity. Reproduced from [71]. CC BY 4.0.

crystal [114] and summarized them in figure 28. A pronounced difference was found between the liquid and crystal data for the O–Er–O and Er–O–Er distributions. The O–Er–O bond angle distribution exhibits two peaks at  $80^\circ$  and  $140^\circ$ , suggesting that  $\text{ErO}_6$  polyhedra are highly distorted in the liquid. Another interesting feature is that the Er–O–Er bond angle distribution exhibits a peak at  $\sim 180^\circ$  in addition to the peak at  $\sim 90^\circ$ , which is not observed for the crystal [114] or in  $l\text{-ZrO}_2$  [70]. This two-peak structure in the Er–O–Er bond angle distribution indicates the formation of a distorted  $\text{OEr}_4$  tetracluster network, whereas tetraclusters are symmetric (comprising regular tetrahedra) in the crystalline phase. This behaviour suggests that the coordination of  $\text{OEr}_4$  tetraclusters is more octahedral-like and hence tolerant of disorder even in the liquid owing to the distortion, providing a linear arrangement manifested by a prominent peak observed at  $180^\circ$  in the Er–O–Er bond angle distribution. This is clearly visible in figure 27(b), where linear atomic arrangements are highlighted by the magenta lines.

To shed light on the similarity in topology between the crystal and liquid phases, we calculated the PD for  $l\text{-Er}_2\text{O}_3$  and compared it with the crystal data in figure 29. The figures show the similarity between the crystal and liquid phases. In particular, neither the Er-centric nor O-centric PDs for  $l\text{-Er}_2\text{O}_3$  shows a vertical profile along the death axis, which is a pronounced

feature in a typical GFL such as  $l\text{-SiO}_2$  [89]. The short lifetime of the profile manifested by the small death value demonstrates that both the crystal and liquid phases exhibit a very densely packed structure associated with the formation of tetraclusters in both phases. We suggest that this similarity is a signature of non-GFL behaviour.

### 3.6. Glassy $\text{SiO}_2$ under ultrahigh pressure

High pressure is an essential tool in expanding the capability of disordered materials, and hence, this technique has been widely applied to disordered materials [116, 117]. As mentioned in the previous section, silica ( $\text{SiO}_2$ ) has been known as one of the most fundamental and abundant oxides on Earth, and can usually be found as quartz, silica sand, or silica stone at high purity. Because of this ubiquitous availability and abundance as a resource around the world,  $\text{SiO}_2$  has been extensively utilized as an industrially useful material.  $\text{SiO}_2$  glass, with high corrosion resistance, high thermostability, and high optical transparency, is a prototype network-forming glass that can be easily synthesized by various methods and therefore is a widely used and technologically important material. Polyamorphism in  $\text{SiO}_2$  glass under pressure is one of the most fascinating and puzzling topics in condensed-matter physics and glass science. Several experimental and theoretical studies have been conducted to clarify the details of polyamorphism

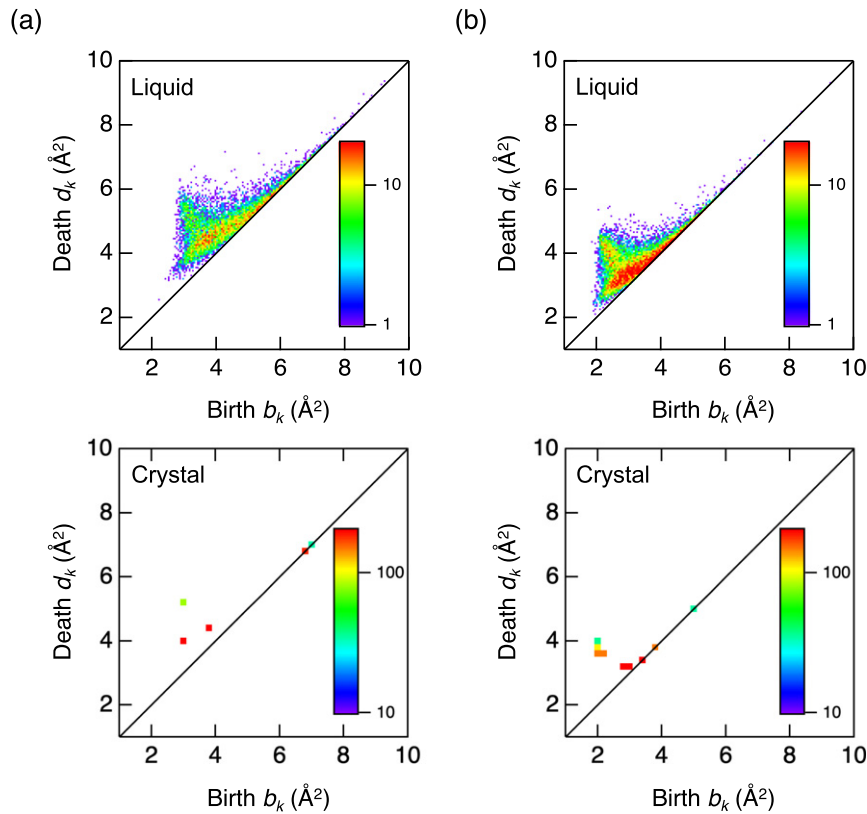


**Figure 29.** PDs of  $\text{Er}_2\text{O}_3$ . (a) Er-centric PD, (b) O-centric PD. Reproduced from [71]. CC BY 4.0.

[117] in  $\text{SiO}_2$  glass under high pressure. However, because of the technical hurdles, the experimental studies have been limited to very low-pressure conditions, preventing a precise understanding of the pressure effect.

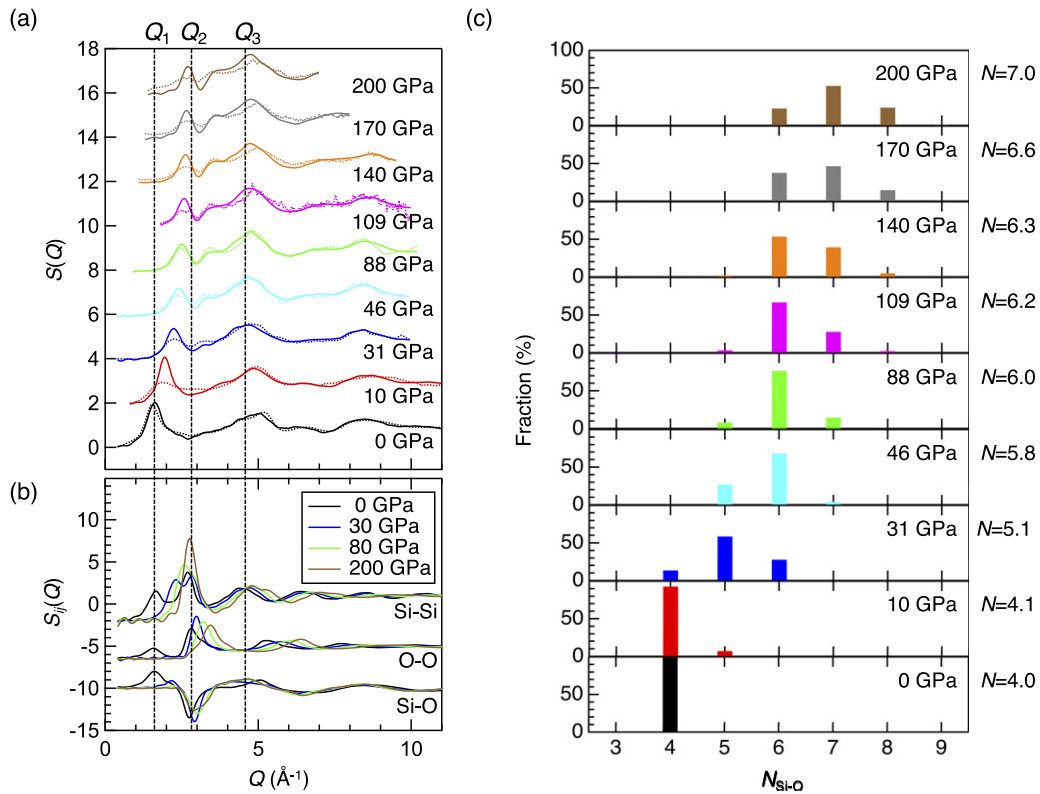
In this section, we report the results of state-of-the-art topological analysis on the basis of atomic configuration obtained by classical MD simulations up to 200 GPa. *In situ* synchrotron high-pressure XRD measurements support the reliability of the simulation. Our supporting analytical methods include the concept of persistent homology and we have placed a special focus on the nature of atomic structure and homology as a function of pressure. Furthermore, we have put emphasis on a general understanding of pressure-induced modification in the glass structure at an intermediate-range scale to illustrate a concept for densification under extremely high pressures, in comparison with crystalline phases.

Figure 30(a) shows the x-ray total structure factors,  $S(Q)$ , measured up to 200 GPa, together with  $S(Q)$  derived from the MD simulations [16]. The experimental  $S(Q)$  are well reproduced by the simulation, although the height of the FSDP observed at  $1.5 < Q < 2.7 \text{ \AA}^{-1}$  is overestimated in the MD simulations (especially for 10 GPa). The observed FSDP position shows a drastic and almost linear increase up to 31 GPa, and the FSDP diminishes beyond this point, which is in line with the results of previous studies, at least up to 100 GPa [118–121]. The second PP observed at around  $Q \sim 3 \text{ \AA}^{-1}$ , which was previously considered as a manifestation of the presence of octahedrally (sixfold)-coordinated Si [118], becomes prominent above 31 GPa, and the peak position

gradually shifts to a higher  $Q$  region with increasing pressure up to 170 GPa. As can be seen in figure 30(b), this behaviour is well understood in terms of partial structure factors,  $S_{ij}(Q)$  [16], in which the evolution of the silicon–silicon PP increases with increasing pressure.

The distributions of Si–O coordination numbers were derived from the MD simulations and are shown in figure 30(c) [16] where the gradual changes from fourfold to higher coordination can be clearly observed. The fourfold-coordinated structure remains up to 10 GPa almost as a single coordination species. The fivefold-coordinated structure becomes predominant at 31 GPa. The dominant coordination state subsequently shifts to sixfold in the pressure range between 46 and 109 GPa. Here, a significant rise in the proportion of sevenfold coordination is observed, whereas the fraction of fivefold-coordinated configuration decreases as a compensation. Such a coordination number change with pressure agrees well with the previous results up to 109 GPa [118–120] and up to 174 GPa [122]. However, it is found that the fraction of the sevenfold-coordination state increases up to 40% at 140 GPa and eventually becomes greater than that of the sixfold-coordination state above 170 GPa, reaching a fraction of 53% at 200 GPa. The noteworthy feature shown here is that the  $\text{SiO}_2$  glass does not comprise a single coordination state but exhibits a broader distribution above 31 GPa, such as  $\text{SiO}_6$  and  $\text{SiO}_7$  polyhedra. Furthermore, the average coordination number is found to change gradually as the coordination distributions evolve. While the observed trend in the Si–O bond length at pressures approaching 140 GPa indicates a stable





**Figure 30.** High-pressure structural data and pressure evolution of Si–O coordination number of SiO<sub>2</sub> glass. (a) X-ray total structure factors,  $S(Q)$ , of SiO<sub>2</sub> glass up to pressures of 200 GPa. Dotted curves: experimental data; solid curves: MD simulations. (b) Faber–Ziman partial structure factors  $S_{\text{SiSi}}(Q)$ ,  $S_{\text{SiO}}(Q)$ , and  $S_{\text{OO}}(Q)$  up to 200 GPa. The approximate principal peak positions labelled by  $Q_1$ ,  $Q_2$ , and  $Q_3$  observed under ambient conditions are indicated by the vertical broken lines. (c) Distribution of the Si–O coordination number in SiO<sub>2</sub> glass as a function of pressure up to 200 GPa. The  $N$  denotes the average Si–O coordination number at each pressure. Reprinted figure with permission from [16], Copyright (2019) by the American Physical Society.

sixfold-coordination state, which behaves as the crystalline form of silica, the trend of showing a constant value above 170 GPa can be interpreted as indicating the onset of an average coordination number higher than 6. The corresponding snapshot of the local environment around oxygen atoms at 200 GPa constructed on the basis of the results of the MD simulation (figure 31(a) [16]) highlights the formation of triclusters (OSi<sub>3</sub>) and/or tetraclusters (OSi<sub>4</sub>). Moreover, Voronoi polyhedral analysis [123] also suggests the formation of the SiO<sub>6</sub> and SiO<sub>7</sub> polyhedra. With a careful inspection of such polyhedral atomic configurations, it is found that the Si–O polyhedra exhibit a large variety of distorted features that deviate from the ideal regular polyhedral structures.

To uncover the atomic structure in SiO<sub>2</sub> glass at high pressures, bond angle distributions with pressure were calculated, and they are shown as O–Si–O and Si–O–Si configurations in figure 31(b) [16]. The O–Si–O bond angle distribution at 0 GPa shows a sharp maximum close to 109.4°, as expected for a regular SiO<sub>4</sub> tetrahedron. The maximum peak position gradually decreases to 90° up to 83 GPa, and the peak distribution becomes distorted with a broad shoulder at angles above 110°. Although the sixfold-coordinated structure is presumed to be the dominant component at 83 GPa, the corresponding angle distributions largely deviate from the ideal O–Si–O angle of 90° for a regular octahedron. The broad feature is consistent with the broad Si–O coordination number distribution

at high pressure (figure 30(c) [16]), indicating that the changes in bond angle distributions are due to the wide variety of O coordination around Si at high pressures.

The features of O–Si–O bond angles at 200 GPa distinctively differ from those observed at lower pressures. The peaks observed at around 75° and 145° are highly analogous to those observed in the random packing structure of hard spheres, indicating that the structure of SiO<sub>2</sub> glass under ultrahigh pressure is very different from that at ambient pressure. Taking into account the results for the short-range structure, the appearance of such peak/shoulders correlates with the formation of sevenfold or higher coordinated structures in a highly distorted polyhedral geometry, which is consistent with the results of Voronoi analysis. The Si–O–Si bond angle distribution shows a peak towards 180° up to 10 GPa, which is a signature of a tetrahedral network motif. On the other hand, the position of the peak shifts to a small-angle region from 31 GPa, and there are two peaks at around 103° (OSi<sub>4</sub> tetracluster) and 124° (OSi<sub>3</sub> tricluster) at 140 GPa. The latter peak is not obvious at 200 GPa, indicating that the OSi<sub>4</sub> tetracluster becomes more dominant.

Figures 32(a)–(g) [16] show Si-centric PDs,  $D(\text{Si})_1$ , that describe the geometrical features of silicon atoms for the topological dimensionality of 1 (rings). We compare 0, 31, 83, and 200 GPa data together with data for stishovite ( $d = 4.28 \text{ g cm}^{-3}$ ) [124],  $\alpha$ -PbO<sub>2</sub>-type ( $d = 4.30 \text{ g m cm}^{-3}$ ) [125],

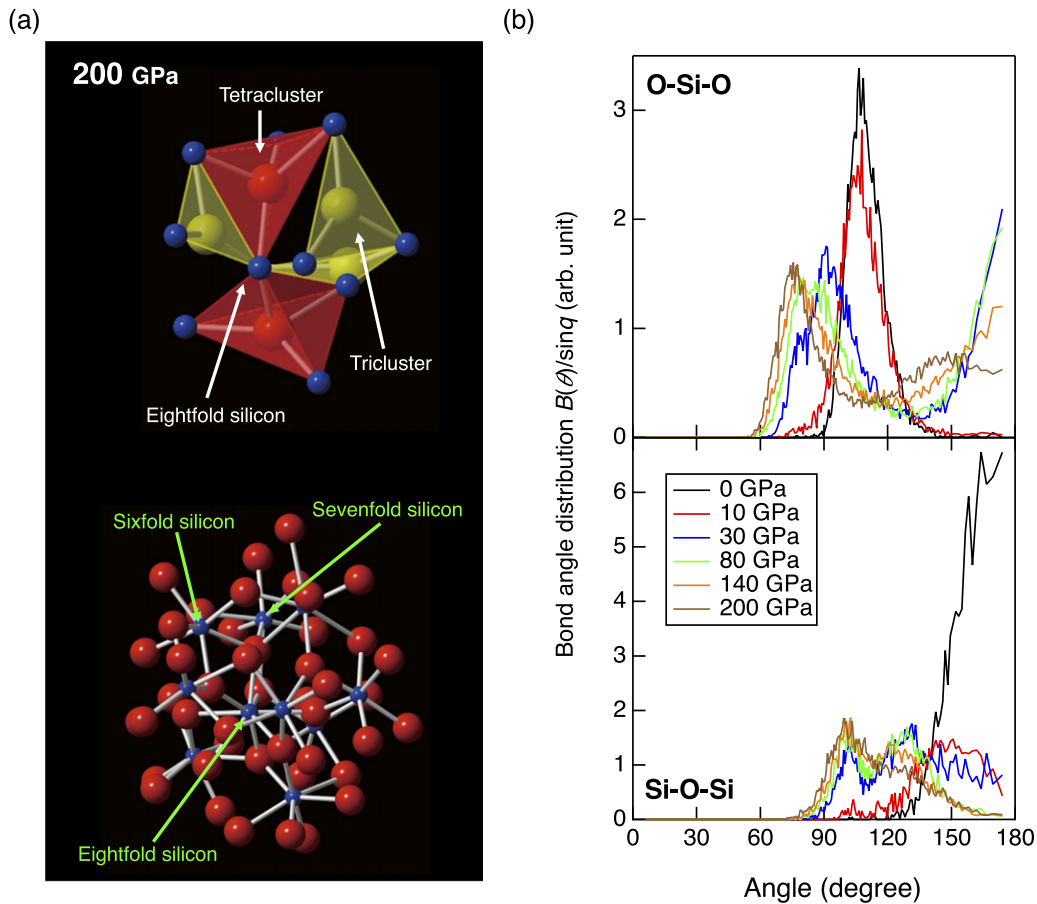


**Figure 31.** Atomic structure and bond angle distribution of SiO<sub>2</sub> glass under high pressure. (a) Snapshot of the local environment around oxygen atoms at 200 GPa, highlighting the oxygen triclusters and tetraclusters configurations (O coordinated with three or four silicon atoms). Blue spheres: silicon atoms; yellow and red spheres: oxygen atoms. (b) Pressure dependence of the O–Si–O (top) and Si–O–Si (bottom) bond angle distributions up to 200 GPa. Reprinted figure with permission from [16], Copyright (2019) by the American Physical Society.

and pyrite-type ( $d = 6.58 \text{ g cm}^{-3}$ ) phases [126]. The profiles along with the death axis highlighted by colours are shown in figure 32(h) [16]. In the case of the crystalline phase, there is a systematic peak shift to small death values with increasing density. It is found that a vertical and broad profile along with the death axis observed at birth of  $2.6 \text{ \AA}^2$  at ambient pressure in the glass almost disappears at 31 GPa and an intense profile in both vertical and horizontal directions is observed near the diagonal at birth of  $3 \text{ \AA}^2$ . This behaviour is a good descriptor for FSDP and is consistent with the formation of triclusters and tetraclusters under high pressures. Moreover, the peak of glass at 200 GPa is very close to pyrite-type data, although the density of the glass is much smaller than the crystalline phase.

The O-centric PDs  $D(\text{O})_2$  (figures 33(a)–(g) [16]), which describe the geometrical features of the oxygen atoms for the topological dimensionality of 2 (cavities), show that some data initially distributed along the diagonal at lower pressure gradually deviate in a direction towards the upper left from the diagonal with pressure, and eventually, appear to form the isolated clusterlike ‘island’ at 200 GPa apart from the original distribution. The profiles along with the diagonal highlighted

by colours are shown in figure 33(h) [16], which shows similar behaviour to that of silicon atoms. With the analyses of persistent homology, the emergence of such an ‘islandlike’ deviation is found to correspond to the formation of the octahedrally coordinated oxygen atoms (that is, SiO<sub>6</sub>), whereas the distribution along the diagonal suggests the presence of oxygen tetrahedra (SiO<sub>4</sub>). This interpretation is highly compatible with our earlier findings. In addition, recent topological analyses for metallic glass with a highly dense-packed structure [49] also showed a very similar topological feature in PDs to that obtained under the high-pressure condition in this study, again demonstrating that densification is achieved through the gradual transition from a network structure to a dense-packed structure in conjunction with a change in the coordination state.

As can be seen in figure 30(b), the partial structure factor for Si–Si,  $S_{\text{SiSi}}(Q)$ , is highly sensitive to pressures above 31 GPa, while that of the PP in  $S_{\text{OO}}(Q)$  is highly insensitive, which is strongly correlated with the pressure-induced changes in PDs,  $D_1$  and  $D_2$ , respectively. These behaviours are also very different from those in densification at lower pressures reported by Zeidler *et al* [127].

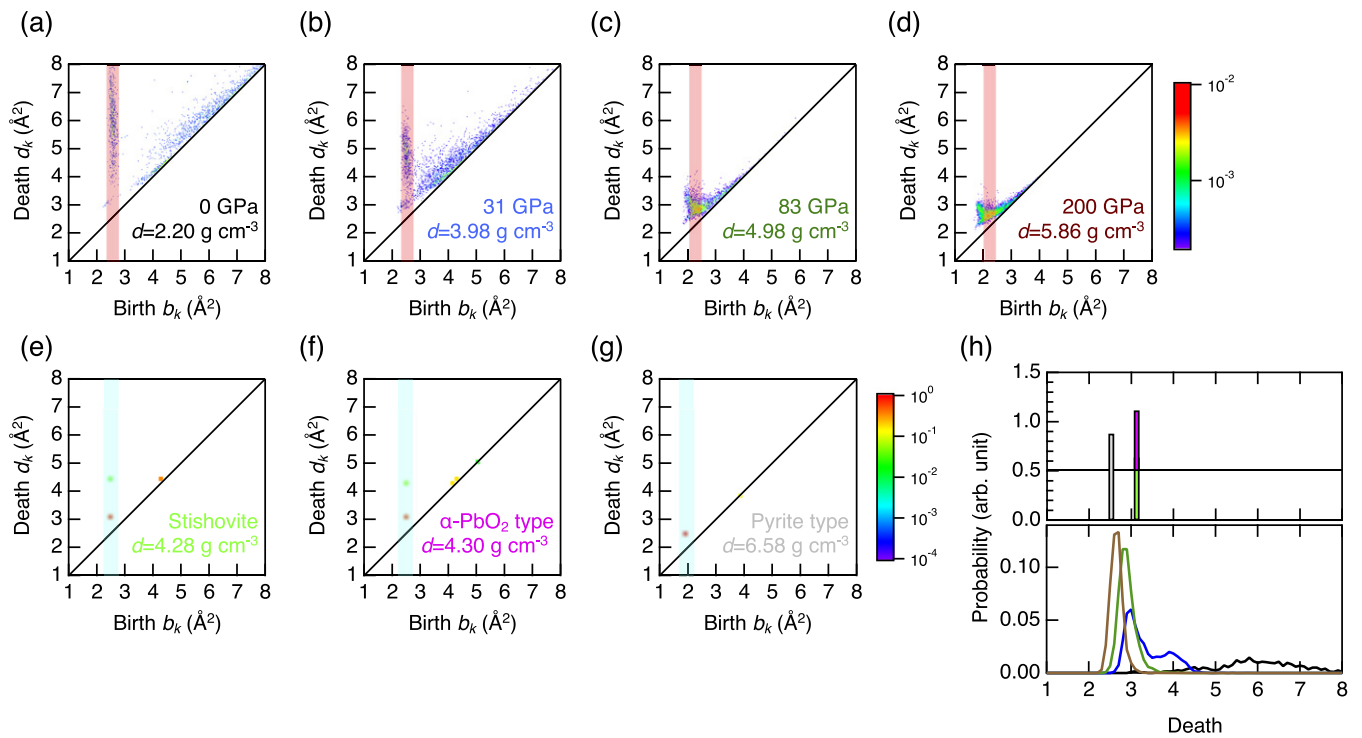


**Figure 32.** Analysis using Si-centric persistent homology for the topological dimensionality of 1. (a)–(g) Si-centric PDs  $D(\text{Si})_1$  at 0, 31, 83, and 200 GPa. (h) Probability profiles along with the death line highlighted by colours. Black line: 0 GPa; blue line: 31 GPa; green line: 83 GPa; and brown line: 200 GPa. Light green: stishovite; pink:  $\alpha$ -PbO<sub>2</sub>-type SiO<sub>2</sub>; grey: pyrite-type SiO<sub>2</sub>. Reprinted figure with permission from [16], Copyright (2019) by the American Physical Society.

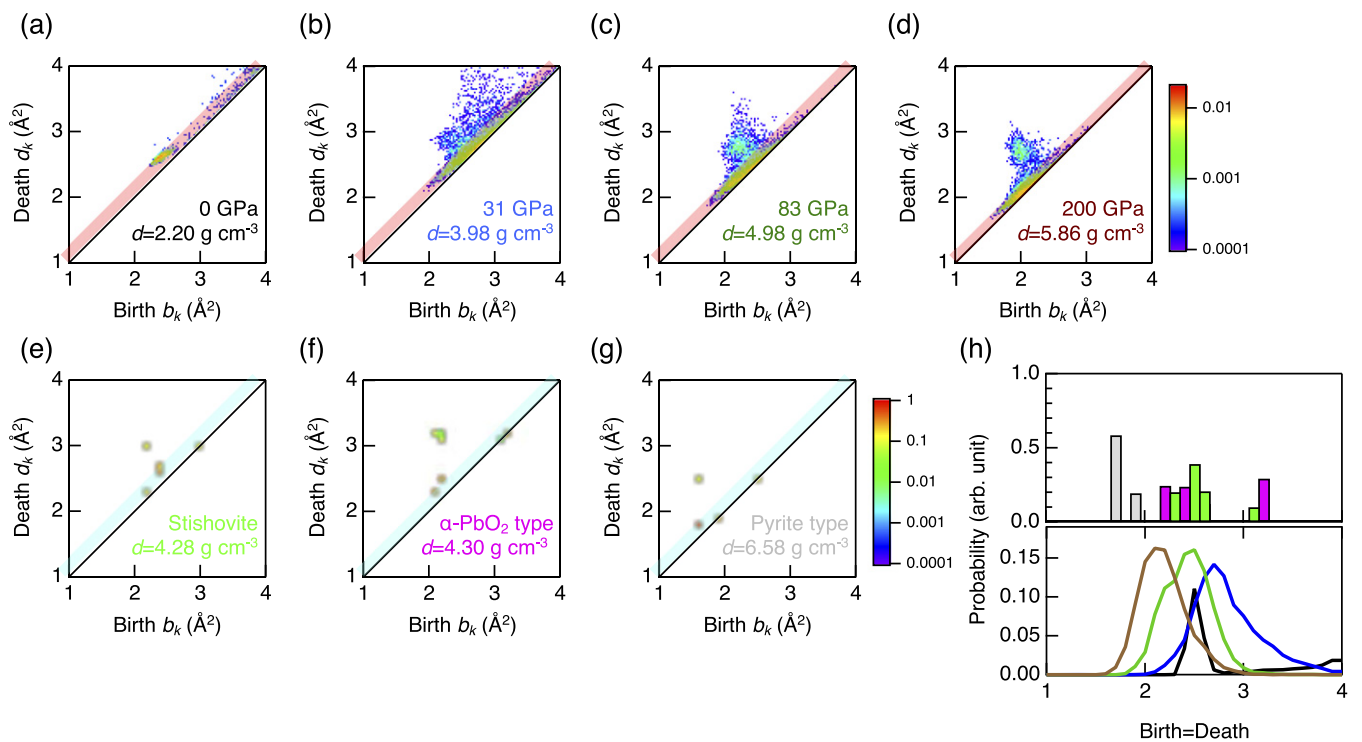


**Figure 33.** Analysis using O-centric persistent homology for the topological dimensionality of 2. (a)–(g) O-centric PDs for  $D(\text{O})_2$  at 0, 31, 83, and 200 GPa. (h) The probability profiles along with the diagonal line highlighted by colours. Black line: 0 GPa; blue line: 31 GPa; green line: 83 GPa; and brown line: 200 GPa. Light green: stishovite; pink:  $\alpha$ -PbO<sub>2</sub>-type SiO<sub>2</sub>; grey: pyrite-type SiO<sub>2</sub>. Reprinted figure with permission from [16], Copyright (2019) by the American Physical Society.

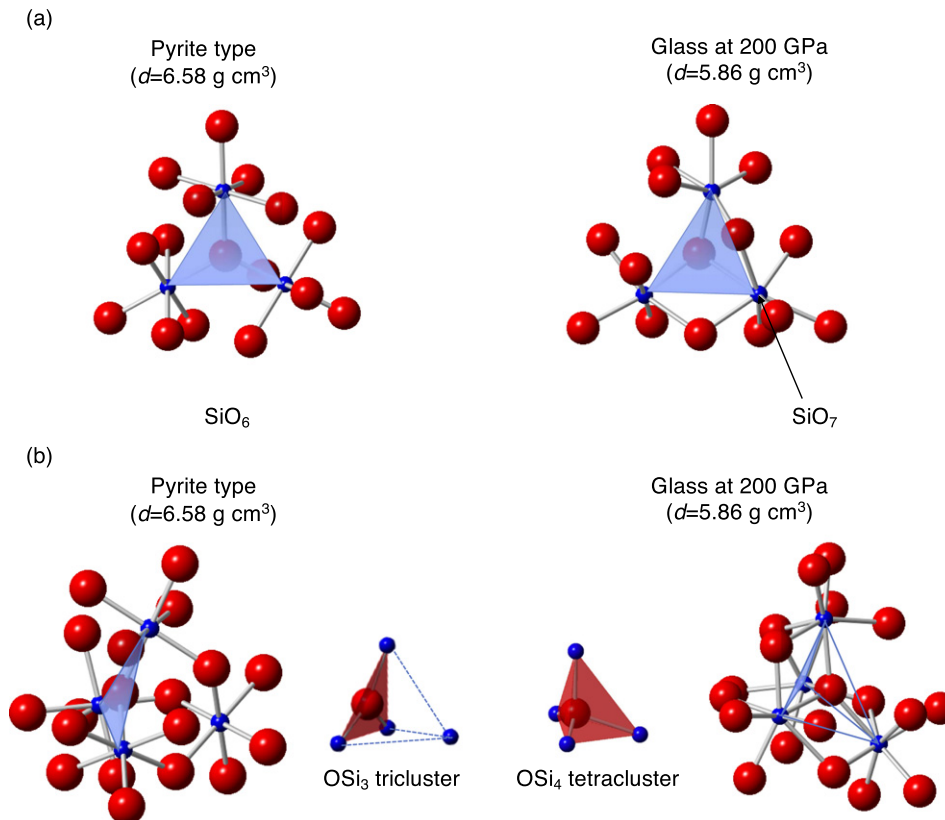


**Figure 34.** Local structures of pyrite-type crystalline  $\text{SiO}_2$  and  $\text{SiO}_2$  glass (at 200 GPa) extracted from PD. (a)  $\text{SiO}_x$  polyhedra extracted from Si-centric persistent homology for the topological dimensionality of 1. (b)  $\text{OSi}_y$  clusters extracted from Si-centric persistent homology for the topological dimensionality of 2. Reprinted figure with permission from [16], Copyright (2019) by the American Physical Society.

Recently, Zeidler *et al* [128] proposed a groundbreaking concept for the relationship between coordination number and oxygen packing fraction (OPF) in oxide glasses, which gives a universal picture of the evolution of the coordination number under pressure. This concept is highly supported by the recent high-pressure experimental results on  $\text{GeO}_2$  glass up to 100 GPa [129], strengthening the predictability of this concept towards configurations under extreme pressures. According to the results of extrapolated calculations for OPF in  $\text{SiO}_2$  glass from previous calculations [120, 121, 127], the onset pressure where the Si–O coordination number becomes higher than 6 is expected to be around 108 GPa [129]. This behaviour is consistent with our previous results for sound velocity as well [130].

To understand the topology in silica glass under ultrahigh pressures, we extract the atomic configurations that give an intense multiplicity for  $D(\text{Si})_1$  and  $D(\text{Si})_2$  of pyrite-type crystal and glass at 200 GPa and show them in figures 34(a) and (b) [16], respectively. Intriguingly, PD analyses provide us with information about triclusters and tetraclusters from  $D(\text{Si})_1$  and  $D(\text{Si})_2$ , respectively. Pyrite-type crystal is composed of only  $\text{SiO}_6$  octahedra ( $\text{OSi}_3$  tricluster). On the other hand, the formation of  $\text{SiO}_7$  polyhedra as well as  $\text{SiO}_6$  octahedra, is observed in the glass, but its topology is very similar to that of pyrite-type crystal (see figure 34(a)). As can be seen in figure 34(b), tricluster in pyrite-type crystal can be extracted by the PD anal-

ysis (see left panel), while the formation of  $\text{OSi}_4$  tetraclusters is observed in the glass at 200 GPa (right panel). However, it is found that the tetracluster is highly distorted (oxygen atom is off centre), and the topology is very similar to that of  $\text{OSi}_3\text{Si}$ , in pyrite-type crystal. It is concluded that the topological similarity between glass at 200 GPa and pyrite-type crystal may be caused by the distortion of oxygen clusters and the variety of Si–O coordination in terms of disorder in glass.

#### 4. Conclusions

In this article, we introduced the instrumentations of hard x-rays for the structural study of disordered materials developed at SPring-8 in the last 20 years. Indeed, the advent of the third-generation synchrotron radiation sources with the development of advanced insertion devices allows us to perform the structural measurement under high temperature and high pressure. Combining quantum beam measurements and advanced simulations with topological analyses would be a very promising way to extract the hidden order in disordered materials [72, 131]. The results of advanced analysis give rise to the capability to forge a new path for designing novel functional disordered materials. The use of coherent x-rays [132] under high temperature and high pressure will promote cutting-edge science in disordered materials.



## Acknowledgments

It is a pleasure to thank László Pusztai for fruitful discussion. The synchrotron radiation experiments were performed under the approval of the Japan Synchrotron Radiation Research Institute (JASRI) (Proposal Nos. 2019A2058, and 2019B2091). This research was supported by JSPS KAKENHI Grant Numbers 20H05878 (to SK) and 20H05881 (to YO and SK).

## ORCID iDs

Koji Ohara  <https://orcid.org/0000-0002-3134-512X>  
 Yohei Onodera  <https://orcid.org/0000-0002-3080-6991>  
 Motohiko Murakami  <https://orcid.org/0000-0002-2165-2994>  
 Shinji Kohara  <https://orcid.org/0000-0001-9596-2680>

## References

- [1] Egelstaff P A 1983 *Adv. Chem. Phys.* **53** 1–6
- [2] Kohara S and Salmon P S 2016 *Adv. Phys. X* **1** 640–60
- [3] Kohara S 2017 *J. Ceram. Soc. Japan* **125** 799–807
- [4] Onodera Y *et al* 2019 *J. Ceram. Soc. Japan* **127** 853–63
- [5] Poulsen H F, Neufeind J, Neumann H-B, Schneider J R and Zeidler M D 1995 *J. Non-Cryst. Solids* **188** 63–74
- [6] Fischer H E, Barnes A C and Salmon P S 2006 *Rep. Prog. Phys.* **69** 233–99
- [7] Waseda Y 2002 *Anomalous X-ray Scattering for Materials Characterization* (Heidelberg: Springer)
- [8] McGreevy R L and Pusztai L 1988 *Mol. Simul.* **1** 359–67
- [9] Soper A K 1996 *Chem. Phys.* **202** 295–306
- [10] Faber T E and Ziman J M 1965 *Phil. Mag.* **11** 153–73
- [11] Isshiki M, Ohishi Y, Goto S, Takeshita K and Ishikawa T 2001 *Nucl. Instrum. Methods A* **467–468** 663–6
- [12] Sakurai Y 1998 *J. Synchrotron Radiat.* **5** 208–14
- [13] Sakata O *et al* 2003 *Surf. Rev. Lett.* **10** 543–7
- [14] Hirao N, Kawaguchi S I, Hirose K, Shimizu K, Ohtani E and Ohishi Y 2020 *Matter Radiat. Extremes* **5** 018403
- [15] Temleitner L, Pusztai L, Akahama Y, Kawamura H, Kohara S, Ohishi Y and Takata M 2008 *Phys. Rev. B* **78** 014205
- [16] Murakami M *et al* 2019 *Phys. Rev. B* **99** 045153
- [17] Katayama Y, Mizutani T, Utsumi W, Shimomura O, Yamakata M and Funakoshi K-i 2000 *Nature* **403** 170–3
- [18] Inamura Y, Katayama Y, Utsumi W and Funakoshi K 2004 *Phys. Rev. Lett.* **93** 015501
- [19] Katayama Y, Hattori T, Saitoh H, Ikeda T, Aoki K, Fukui H and Funakoshi K 2010 *Phys. Rev. B* **81** 014109
- [20] Kohara S, Suzuya K, Kashiwara Y, Matsumoto N, Umesaki N and Sakai I 2001 *Nucl. Instrum. Methods Phys. Res. A* **467–468** 1030–3
- [21] Kohara S and Suzuya K 2003 *Nucl. Instrum. Methods Phys. Res. B* **199** 23–8
- [22] Kohara S, Itou M, Suzuya K, Inamura Y, Sakurai Y, Ohishi Y and Takata M 2007 *J. Phys.: Condens. Matter* **19** 506101
- [23] Kohara S *et al* 2016 *Z. Phys. Chem.* **230** 339–68
- [24] Ohara K *et al* 2020 *Int. J. Microgravity Sci. Appl.* **37** 370202
- [25] Maréchal X-M, Hara T, Tanabe T, Tanaka T and Kitamura H 1998 *J. Synchrotron Radiat.* **5** 431–3
- [26] Yamaoka H, Hiraoka N, Ito M, Mizumaki M, Sakurai Y, Kakutani Y, Koizumi A, Sakai N and Higashi Y 2000 *J. Synchrotron Radiat.* **7** 69–77
- [27] Ohara K *et al* 2020 *J. Synchrotron Radiat.* **25** 1627–33
- [28] Hosokawa S, Wang Y, Bézar J-F, Greif J, Pilgrim W-C and Murase K 2002 *Z. Phys. Chem.* **216** 1219
- [29] Price D L 2010 *High-Temperature Levitated Materials* (Cambridge: Cambridge University Press)
- [30] Winborne D A, Nordine P C, Rosner D E and Marley N F 1976 *Metall. Mater. Trans. B* **7** 711–3
- [31] Rhim W K, Chung S K, Barber D, Man K F, Gutt G, Rulison A and Spjut R E 1993 *Rev. Sci. Instrum.* **64** 2961–70
- [32] Masaki T *et al* 2007 *Rev. Sci. Instrum.* **78** 026102
- [33] Weber J K R, Rey C A, Neufeind J and Benmore C J 2009 *Rev. Sci. Instrum.* **80** 083904
- [34] Benmore C J and Weber J K R 2011 *Phys. Rev. X* **1** 011004
- [35] Akahama Y and Kawamura H 2004 *J. Appl. Phys.* **96** 3748–51
- [36] Mao H K, Xu J and Bell P M 1986 *J. Geophys. Res.* **91** 4673–6
- [37] Roux S and Jund P 2010 *Comput. Mater. Sci.* **49** 70–83
- [38] Roux S L and Jund P 2011 *Comput. Mater. Sci.* **50** 1217
- [39] King S V 1967 *Nature* **213** 1112–3
- [40] Guttman L 1990 *J. Non-Cryst. Solids* **116** 145–7
- [41] Franzblau D S 1991 *Phys. Rev. B* **44** 4925–30
- [42] Goetzke K and Klein H-J 1991 *J. Non-Cryst. Solids* **127** 215–20
- [43] Yuan X and Cormack A N 2002 *Comput. Mater. Sci.* **24** 343–60
- [44] Wooten F 2002 *Acta Crystallogr. A* **58** 346–51
- [45] Gupta P K and Cooper A R 1990 *J. Non-Cryst. Solids* **123** 14–21
- [46] Ono M, Hara K, Fujinami M and Ito S 2012 *Appl. Phys. Lett.* **101** 164103
- [47] Heimbach I, Rhiem F, Beule F, Knodt D, Heinen J and Jones R O 2017 *J. Comput. Chem.* **38** 389–94
- [48] Onodera Y *et al* 2019 *NPG Asia Mater.* **11** 75
- [49] Hiraoka Y, Nakamura T, Hirata A, Escolar E G, Matsue K and Nishiura Y 2016 *Proc. Natl Acad. Sci. USA* **113** 7035–40
- [50] Hirata A, Kang L J, Fujita T, Klumov B, Matsue K, Kotani M, Yavari A R and Chen M W 2013 *Science* **341** 376–9
- [51] Obayashi I 2018 HomCloud [https://wpi-airm.tohoku.ac.jp/hiraoka\\_lab/homcloud/index.en.html/](https://wpi-airm.tohoku.ac.jp/hiraoka_lab/homcloud/index.en.html/) Hiraoka Laboratory, Advanced Institute for Materials Research, Tohoku University, Japan
- [52] Rino J P, Ebbsjö I, Kalia R K, Nakano A and Vashishta P 1993 *Phys. Rev. B* **47** 3053–62
- [53] Kohara S, Akola J, Morita H, Suzuya K, Weber J K R, Wilding M C and Benmore C J 2011 *Proc. Natl Acad. Sci.* **108** 14780–5
- [54] Greaves G N and Sen S 2007 *Adv. Phys.* **56** 1–166
- [55] Salmon P S and Zeidler A 2013 *Phys. Chem. Chem. Phys.* **15** 15286–308
- [56] Kohara S, Suzuya K, Takeuchi K, Loong C-K, Grimsditch M, Weber J K R, Tangeman J A and Key T S 2004 *Science* **303** 1649–52
- [57] Yu J *et al* 2009 *Chem. Mater.* **21** 259–63
- [58] Akola J *et al* 2013 *Proc. Natl Acad. Sci. USA* **110** 10129–34
- [59] Onodera Y, Kohara S, Masai H, Koreeda A, Okamura S and Ohkubo T 2017 *Nat. Commun.* **8** 15549
- [60] Wakihara T, Kohara S, Sankar G, Saito S, Sanchez-Sanchez M, Overweg A R, Fan W, Ogura M and Okubo T 2006 *Phys. Chem. Chem. Phys.* **8** 224–7
- [61] Haines J, Levelut C, Isambert A, Hébert P, Kohara S, Keen D A, Hammouda T and Andraut D 2009 *J. Am. Chem. Soc.* **131** 12333–8
- [62] Hirata A, Kohara S, Asada T, Arai M, Yogi C, Imai H, Tan Y, Fujita T and Chen M W 2016 *Nat. Commun.* **7** 11591
- [63] Kohara S *et al* 2006 *Appl. Phys. Lett.* **89** 201910
- [64] Matsunaga T *et al* 2011 *Nat. Mater.* **10** 129–34
- [65] Ohara K *et al* 2012 *Adv. Funct. Mater.* **22** 2251–7
- [66] Stellhorn J R, Hosokawa S, Kaiser B, Kimura K, Boudet N, Blanc N, Tajiri H, Kohara S and Pilgrim W-C 2021 *Z. Phys. Chem.* **235** 141
- [67] Hosokawa S *et al* 2019 *Phys. Rev. B* **100** 054204

- [68] Hart R, Benmore C J, Neufeind J, Kohara S, Tomberli B and Egelstaff P A 2005 *Phys. Rev. Lett.* **94** 047801
- [69] Skinner L B *et al* 2013 *Phys. Rev. B* **87** 024201
- [70] Kohara S *et al* 2014 *Nat. Commun.* **5** 5892
- [71] Koyama C *et al* 2020 *NPG Asia Mater.* **12** 43
- [72] Onodera Y *et al* 2020 *NPG Asia Mater.* **12** 85
- [73] Nishigaki J, Yamazoe S, Kohara S, Fujiwara A, Kurashige W, Negishi Y and Tsukuda T 2013 *Chem. Commun.* **50** 839–41
- [74] Li B *et al* 2018 *Nat. Mater.* **17** 226–30
- [75] Zachariassen W H 1932 *J. Am. Chem. Soc.* **54** 3841–51
- [76] Sun K-H 1947 *J. Am. Ceram. Soc.* **30** 277–81
- [77] Hannon A C 2021 Basic Concepts of Network Glass Structure *Encyclopedia of Glass Science, Technology, History, and Culture* ed P Richet, R Conradt, A Takada and J Dyon (New York: Wiley Online Library)
- [78] Salmon P S, Martin R A, Mason P E and Cuello G J 2005 *Nature* **435** 75–8
- [79] Wright A C and Leadbetter A J 1976 *Phys. Chem. Glasses* **17** 122–45
- [80] Phillips J C 1981 *J. Non-Cryst. Solids* **43** 37–77
- [81] Price D L, Moss S C, Reijers R, Saboungi M-L and Susman S 1988 *J. Phys. C: Solid State Phys.* **21** 1069L–72
- [82] Elliott S R 1991 *Nature* **354** 445–52
- [83] Wright A C 1994 *J. Non-Cryst. Solids* **179** 84–115
- [84] Salmon P S 1994 *Proc. R. Soc. A* **445** 351–65
- [85] Gaskell P H and Wallis D J 1996 *Phys. Rev. Lett.* **76** 66–9
- [86] Mei Q, Benmore C J, Sen S, Sharma R and Yargar J 2008 *Phys. Rev. B* **78** 144204
- [87] Zeidler A and Salmon P S 2016 *Phys. Rev. B* **93** 214204
- [88] Shi R and Tanaka H 2019 *Sci. Adv.* **5** 3194
- [89] Mei Q, Benmore C J and Weber J K R 2007 *Phys. Rev. Lett.* **98** 057802
- [90] Ojovan M I 2004 *JETP Lett.* **79** 632–4
- [91] Masai H, Kohara S, Onodera Y, Koreeda A, Saito K, Sekiya E H and Kitamura N 2020 *J. Ceram. Soc. Japan* **128** 1038–44
- [92] Takada A, Richet P, Catlow C R A and Price G D 2004 *J. Non-Cryst. Solids* **345–346** 224–9
- [93] Urbain G, Bottinga Y and Richet P 1982 *Geochim. Cosmochim. Acta* **46** 1061–72
- [94] Angell C A 1995 *Science* **267** 1924–35
- [95] Isard J O 1969 *J. Non-Cryst. Solids* **1** 235–61
- [96] Habasaki J, Leon C and Ngai K L 2017 *Dynamics of Glassy, Crystalline and Liquid Ionic Conductors* (Berlin: Springer)
- [97] Wicks J D, McGreevy R L and Börjesson L 1997 *Phase Transit.* **61** 195–213
- [98] Greaves G N 1985 *J. Non-Cryst. Solids* **71** 203–17
- [99] Du J and Corrales L R 2006 *J. Non-Cryst. Solids* **352** 3255–69
- [100] Maekawa H, Maekawa T, Kawamura K and Yokokawa T 1991 *J. Non-Cryst. Solids* **127** 53–64
- [101] Kohara S, Ohno H, Takata M, Usuki T, Morita H, Suzuya K, Akola J and Pusztai L 2010 *Phys. Rev. B* **82** 134209
- [102] Greaves G N and Ngai K L 1995 *Phys. Rev. B* **52** 6358–80
- [103] Park B and Cormack A N 1999 *J. Non-Cryst. Solids* **255** 112–21
- [104] Habasaki J, Okada I and Hiwatari Y 1995 *J. Non-Cryst. Solids* **183** 12–21
- [105] Habasaki J, Okada I and Hiwatari Y 1996 *J. Non-Cryst. Solids* **208** 181–90
- [106] Kim S W, Shimoyama T and Hosono H 2011 *Science* **333** 71–4
- [107] Wuttig M and Yamada N 2007 *Nat. Mater.* **6** 824–32
- [108] Akola J and Jones R O 2008 *J. Phys.: Condens. Matter* **20** 465103
- [109] Greaves G N *et al* 2009 *Science* **322** 566–70
- [110] Barnes A C, Skinner L B, Salmon P S, Bytchkov A, Pozdnyakova I, Farmer T O and Fischer H E 2009 *Phys. Rev. Lett.* **103** 225702
- [111] Greaves G N, Wilding M C, Hennem L, Langstaff D, Kargl F, Benmore C J and Weber J K R 2011 *Phys. Rev. Lett.* **106** 119601
- [112] Tamaru H, Koyama C, Saruwatari H, Nakamura Y, Ishikawa T and Takada T 2018 *Microgravity Sci. Technol.* **30** 643–51
- [113] Salmon P S 2018 *Magma under Pressure: Advances in High-Pressure Experiments on Structure and Properties of Melts* ed Y Kono and C Sanloup (Amsterdam: Elsevier) p 347
- [114] Saiki A, Ishizawa N, Mizutani N and Kato M 1985 *J. Ceram. Assoc. Japan* **93** 649–54
- [115] Bhatia A B and Thornton D E 1971 *Phys. Rev. B* **4** 3004–12
- [116] Greaves G N, Meneau F, Sapelkin A, Colyer L M, ap Gwynn I, Wade S and Sankar G 2003 *Nat. Mater.* **2** 622–9
- [117] El'kin F S, Brazhkin V V, Khvostantsev L G, Tsiok O and Lyapin A G 2002 *J. Exp. Theor. Phys. Lett.* **75** 342–7
- [118] Meade C, Hemley R J and Mao H K 1992 *Phys. Rev. Lett.* **69** 1387–90
- [119] Sato T and Funamori N 2008 *Phys. Rev. Lett.* **101** 255502
- [120] Benmore C J, Soignard E, Amin S A, Guthrie M, Shastri S D, Lee P L and Yarger J L 2010 *Phys. Rev. B* **81** 054105
- [121] Sato T and Funamori N 2010 *Phys. Rev. B* **82** 184102
- [122] Prescher C, Prakapenka V B, Stefanski J, Jahn S, Skinner L B and Wang Y 2017 *Proc. Natl Acad. Sci. USA* **114** 10041–6
- [123] Fukunaga T *et al* 2006 *Intermetallics* **14** 893–7
- [124] Ross N L, Shu J and Hazen R M 1990 *Am. Mineral.* **75** 739–47
- [125] Dera P, Prewitt C T, Boctor N Z and Hemley R J 2002 *Am. Mineral.* **87** 1018–23
- [126] Kuwayama Y, Hirose K, Sata N and Ohishi Y 2005 *Science* **309** 923–5
- [127] Zeidler A *et al* 2014 *Phys. Rev. Lett.* **113** 135501
- [128] Zeidler A, Salmon P S and Skinner L B 2014 *Proc. Natl Acad. Sci.* **111** 10045–8
- [129] Kono Y, Kenney-Benson C, Ikuta D, Shibasaki Y, Wang Y and Shen G 2016 *Proc. Natl Acad. Sci. USA* **113** 3436–41
- [130] Murakami M and Bass J D 2010 *Phys. Rev. Lett.* **104** 025504
- [131] Salmon P S 2002 *Nat. Mater.* **1** 87–8
- [132] Wochner P *et al* 2009 *Proc. Natl Acad. Sci.* **106** 11511–4